IMPROVED PERFORMANCE OF RAILCAR/RAIL TRUCK INTERFACE COMPONENTS

A Thesis

by

BRETT ALAN STORY

Submitted to the Office of Graduate Studies of
Texas A&M University
in partial fulfillment of the requirements for the degree of

MASTER OF SCIENCE

August 2007

Major Subject: Civil Engineering

IMPROVED PERFORMANCE OF RAILCAR/RAIL TRUCK INTERFACE COMPONENTS

A Thesis

by

BRETT ALAN STORY

Submitted to the Office of Graduate Studies of
Texas A&M University
in partial fulfillment of the requirements for the degree of

MASTER OF SCIENCE

Approved by:

Chair of Committee, Gary Fry
Committee Members, Stefan Hurlebaus
Terry Creasy
Head of Department, David Rosowsky

August 2007

Major Subject: Civil Engineering

ABSTRACT

Improved Performance of Railcar/Rail Truck Interface Components. (August 2007)

Brett Alan Story, B.S., Texas A&M University

Chair of Advisory Committee: Dr. Gary T. Fry

The objective of this research is to improve the railcar/rail truck interface by developing a low maintenance bearing interface with a favorable friction coefficient. Friction and wear at the center bowl/center plate bearing interface cause high turning moments around curved track, wear of truck components, and increased detrimental dynamic effects.

The recommended improvement of the rail truck interface is a set of two steel inserts, one concave and one convex, that can be retrofit to center bowls/center plates. The insert geometry addresses concerns about maintaining favorable pressure distribution on existing components, minimizing overall height increase to accommodate existing infrastructure, and retaining railcar stability. The stability of the railcar upon the design inserts has been ensured when the instantaneous center of rotation of the railcar body is above the railcar center of gravity. The damping ratio provided by the frictional moment within center bowl is 240 and eliminates the possibility of dynamic amplification.

Using a 90 inch radius of curvature ensures stability and requires a 0.5 inch diameter reduction of the existing center plate for a gap of 1/16 inch. The increase in railcar height for the specific design is 0.71 inches which can be absorbed by either grinding of the center plate or new manufacturing dimensions. The design is feasible for small travel values corresponding to small vertical gaps at the side bearings.

In addition to geometry alterations, the bearing surfaces are coated with a protective metallic layer. The literature suggests that optimum friction coefficients between bearing elements in the center bowl/center plate interface may reduce turning moments of the truck, wear of truck components, and detrimental dynamic effects such

as hunting. Axial-torsional tests determined friction coefficient estimates and wear properties for a matrix of various metallic protective coatings and steel. Tungsten carbide-cobalt-chrome has a favorable coefficient of 0.3 under standard center bowl/center plate contact conditions.

DEDICATION

To my family

ACKNOWLEDGEMENTS

Several people have made numerous sacrifices to help accomplish the goals of this research project. I would like to begin by thanking the members of my thesis committee, Dr. Stefan Hurlebaus, Dr. Terry Creasy, and my committee chair, Dr. Gary Fry, for their input and guidance with this research project. In addition to the guidance of my professors, I am also in debt to my research group for their constant positive critique and encouragement. I would also like to thank Matt Potter and Dr. Peter Keating of the High Bay Structural and Materials Testing Laboratory whose experience and technical expertise ensured successful testing. In addition, I would like to thank John Winne of Hitemco Southwest for his donation of time and resources to coat test specimens. Cheryl Burt, of the Texas Transportation Institute, provided invaluable assistance and guidance in the acquisition of testing and research materials. I am thankful to Dr. Loren Lutes, who provided a unique and unmatched view of the dynamics associated with the project.

I would like to thank the American Association of Railroads and Transportation Technology Center, Inc. for both their financial support of this research, and the opportunity to work with David Davis and Dr. Harry Tournay.

Lastly, I am extremely thankful for my family and their support throughout my college career. Without their endless encouragement and sacrifice, my success would have been impossible.

TABLE OF CONTENTS

Page

CHAPTER Page

LIST OF FIGURES

Page

Page

Page

LIST OF TABLES

Page

NOMENCLATURE

a	distance from center bowl center to outer side bearing edge
A	area
AAR	Association of American Railroads
b_1	height of side bearing from bolster face
B_r	width of railcar
c_{eq}	equivalent damping coefficient
c_{cr}	critical damping
C	100’ chord length for rail curve
$C’$	40’ chord length defined by railcar length
C.G.	center of gravity
d	diameter of center bowl
D	degree of curvature encompassed by C
DOF	degree of freedom
$D’$	degree of curvature encompassed by C’
FBD	free body diagram
EOM	equation of motion
E_L	energy contained in hysteresis loops
g	vertical side bearing gap
g_a	acceleration of gravity
h	horizontal gap between vertical center plate and center bowl faces
H	horizontal friction force
H_r	railcar height
I.C.	instantaneous center of rotation
J	mass moment of inertia
L	moment arm of frictional moment
L_1	vertical distance between I.C. and upper face of lower side bearing
L_2	vertical distance between I.C. and lower face of upper side bearing

L_3	radius of center bowl
L_4	radius of center plate inserts
m	slope of unloading line
M_f	friction moment
N	normal force
N_v	normal component of pressure resultant
p	pressure distribution
P_s	scale railcar force
P_T	scaled axial load for laboratory testing
r	radial polar coordinate
R	radius of curvature of rail curve
R_1	radius of curvature of spherical insert face
R_2	radius from I.C. to outermost edge of side bearing
R_{cg}	distance from I.C. to C.G.
S	arc length
S_1	outer arc length
S_2	inner arc length
t_i	inner thickness of center bowl insert
t_f	final time
T	torque
TTC	Transportation Technology Center, Inc. test facility
TTCI	Transportation Technology Center, Inc.
W	railcar weight
W_E	work energy
α	difference between γ and θ1
β	angle enclosed by center bowl inner face from vertical
γ	angle enclosed by outer side bearing edge from vertical
Δ_1	lead angle encompassed by railcar center line and R
Δ_2	rear angle encompassed by railcar center line and R

ΔH	change in railcar height
ζ	damping ratio
θ	angle of rotation (roll) of railcar
θ_0	initial angle of rotation
θ_1	railcar body rotation required for closure of vertical side bearing gap
θ_2	railcar body rotation required for closure of horizontal center bowl gap
θ_a	angular polar coordinate
θ_z	angle of twist (yaw) of railcar
θ_{z1}	angle of twist of lead truck
θ_{z2}	angle of twist of rear truck
θ_{zmax}	maximum angle of twist (yaw) of railcar
μ	friction coefficient
σ	stress
σ_B	stress in center bowl
σ_T	stress traction
τ	shear stress
φ	difference between β and θ2
φ_s	vertical spherical angular coordinate
φ_z	test rotation coordinate
ω	natural frequency

CHAPTER I

INTRODUCTION

1.1 Background

A gondola is a railcar used for transporting bulk materials, such as gravel or coal, at approximately 100 tons per railcar. These loads create a total railcar weight that can exceed 286,000 pounds (Wolf 2005a). As railcar weights increase to improve capacity efficiency, new methods and devices can be implemented to increase railcar performance and service life.

The body of the railcar sits on two wheel and axle suspension assemblies called trucks. The body of the railcar contacts each truck at a center bowl and two side bearings (Hay 1982). The underside of the railcar has two cylindrical center plates that fit into center bowls located on trucks at either end of the railcar as shown in Figures 1.1 and 1.2.

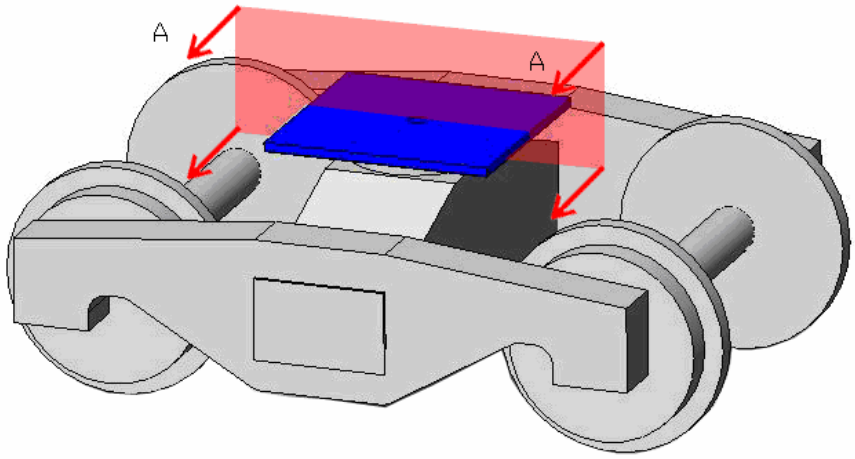

Figure 1.1: Railcar Truck and Center Bowl/Center Plate Assembly

This thesis follows the style of *Journal of Structural Engineering*.

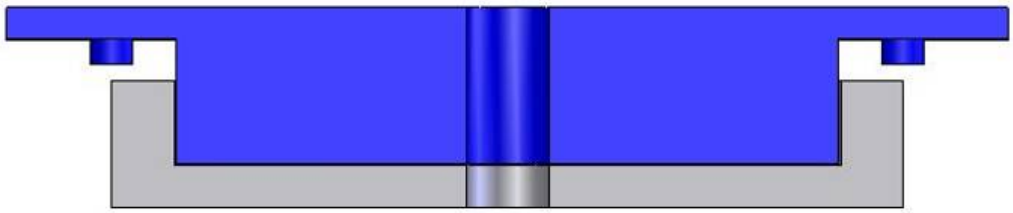

Figure 1.2: Cross Section A-A of Center Bowl/Center Plate Assembly

The center bowl, which takes approximately 90% of the cargo load and railcar self weight, is a cylindrical bowl that contacts the center plate on a flat surface (Tournay et al. 2006). A center pin runs through the middle of the center bowl/center plate assembly and alignments the truck and railcar body during maintenance. The side bearings, which may or may not be in constant contact over various loading conditions, prevent excessive rocking of the railcar (Hay 1982).

Currently, the Association of American Railroads (AAR) requires center bowl liners or other lubricants that reduce friction and wear between the center bowl/center plate bearing surfaces (AAR 1982). Over time, plastic or metallic center bowl liners wear down and must be replaced. Replacement decreases productivity and adds maintenance costs. Research shows that liners fail when center bowl/center plate contact shifts from flat, evenly distributed contact to point or edge contact (Tournay et al. 2006). When point or line contact damages liners, the friction at the bearing surface rises and reduces performance by increasing turning moments. Estimates on this escalated friction coefficient for use in industry simulations are as high as 1.0 (Simson and Pearce 2005).

1.2 Problem Statement

When a railcar enters a curve, the trucks follow the rail and the center plate rotates within the center bowl. The bearing interaction between the center bowl and center plate surfaces causes wear, and increased friction forces between the worn surfaces increase

turning moment. Repeated cornering wears both flat contact surfaces of the center plate and center bowl as well as the rim or wall of the center bowl (Tournay et al. 2006).

Ideally, the center bowl and center plate rotate concentrically about their common geometric center, and wear to the components would distribute equally to make a symmetric pressure distribution. Non-uniform loading conditions, caused by unsymmetrical cargo loads or negotiating curves, cause non-uniform contact between the center plate and center bowl. As a result, the center plate may move away from the geometric center of the center bowl, as illustrated in Figure 1.3. In Figure 1.3, the center of rotation for the center plate has moved from the geometric center of the center bowl (Figure 1.3(a)) to the center bowl rim (Figure 1.3(b)).

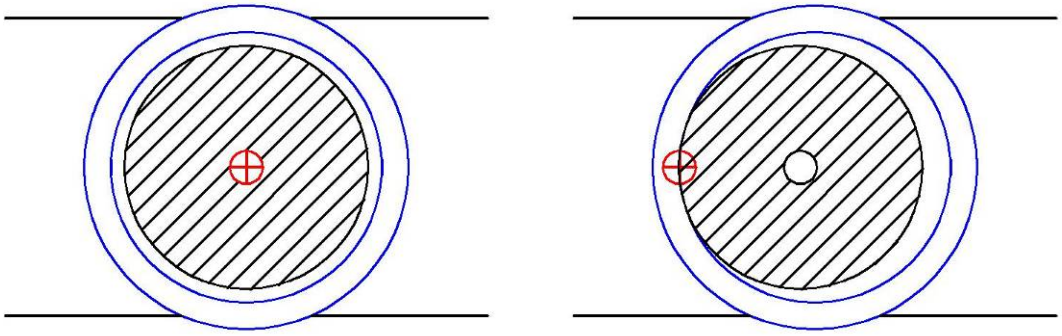

(a) Unworn, Uniform Loading (b) Worn, Uneven Loading

Figure 1.3: Center Plate Rotation Offset from Center Bowl

As a rail truck enters a horizontal curve, the center plate may slide and contact with the wall or rim of the center bowl. Tear down tests performed at Transportation Technology Center (TTC) suggest that similar events may cause point or line contact between the center plate and center bowl; therefore, the rotation between the two surfaces occurs at the contact point, not at their concentric centers (Tournay et al. 2006). This non-concentric rotation leads to uneven bearing contact and pressure distributions resulting in increasingly uneven component wear.

The degradation of center bowl/center plate interfaces has adverse effects on other railcar components. In addition to truck component wear, high turning moments resulting from large friction forces in the center bowl can cause rail wheels to jerk, slip, and grind on the rail on horizontal curves. As the railcar enters a curve, the friction forces within the center bowl and at the side bearings resist truck rotation and thus the wheels on the high side of the rail are forced against the rail. This wheel/rail interaction causes gauge spreading of the track and damages wheel and rail profiles.

Another scenario that wears truck components and rails is hunting. Hunting is a dynamic condition, often occurring in unloaded railcars at moving high speeds, where trucks and their axles rotate rapidly about the center plate and cause wheels to bounce back and forth against the rail (Hay 1982). Extreme hunting can cause the wheel to climb the rail and possibly derail. Low friction at the center bowl/center plate bearing interface does not provide sufficient resistance to hunting; therefore hunting instability results. Other detrimental dynamic effects in the center bowl can be reduced with an appropriate friction coefficient. Impact between the center plate and the center bowl rim is an example of such dynamic interaction. Simulations have shown that center bowl friction coefficients less than 0.3 increase hunting and center bowl rim impacts (Simson and Pearce 2005).

1.3 Project Objective

The project objective is to improve railcar/rail truck interface performance by implementing low maintenance, bearing interfaces with favorable friction coefficients. The design has two features essential to mitigating the center plate/center bowl bearing problem: 1) altered interface geometry and 2) favorable friction coefficient. The design combines two steel inserts, one convex and one concave, with a protective coating on the bearing faces of the inserts. As will be described in detail in Chapter II, the insert geometry reduces edge contact and improves the stress state at the interface. A metallic protective coating on the insert contact faces reduces wear and provides a favorable friction coefficient. Different materials were tested in the laboratory to determine their

friction coefficient estimates and wear properties. From these tests, the proper protective coating can be chosen for the design.

CHAPTER II

GEOMETRIC INSERT DESIGN PROCEDURES

2.1 Insert Geometry

A set of center bowl/center plate bearing inserts is proposed that limits wear caused by stress concentrations by reducing point or edge contact between the center bowl and center plate. A graphic of the general design scheme is shown in Figure 2.1. As a first step in determining the best alternative bearing interface geometry, SolidWorks models of different geometric interfaces were constructed to examine their interaction.

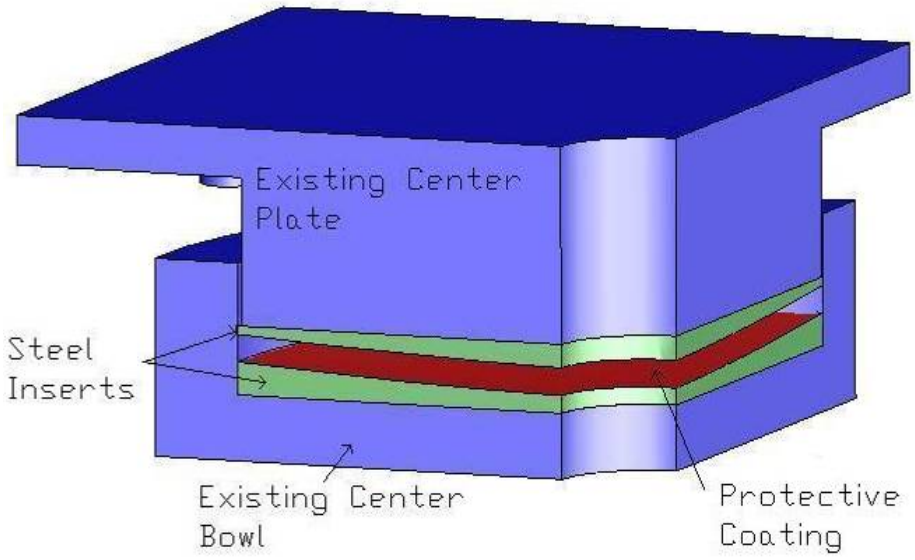

Figure 2.1: Geometric Design of Proposed Inserts

2.2 Investigation of Spherical Interface Geometry

Figure 2.2 shows an exaggerated spherical interface in both the centered and tilted position caused by turning or eccentric loading.

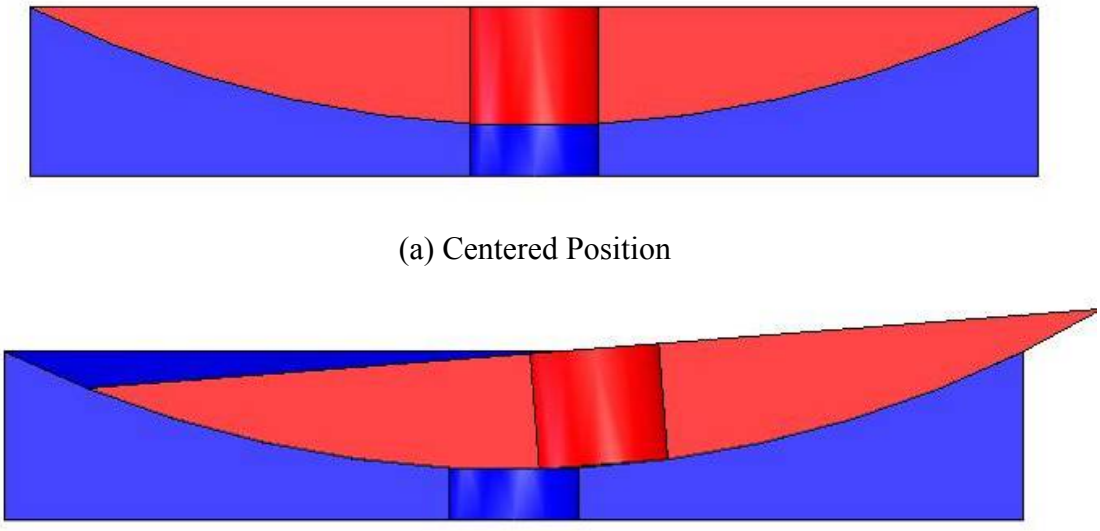

(a) Centered Position

(b) Tilted Position

Figure 2.2: Exaggerated Spherical Bearing Interface

The exaggerated interaction of the spherical bearing surface shows the elimination of point or line contact as the center plate rotates against the center bowl. A lack of edge contact along the faces of the center bowl and center plate reduces concentrated contact stresses. This stress reduction correlates to a wear reduction in the interface components. Depending on the radius of curvature at the interface, the center plate may have a tendency to climb the center bowl and instability may occur. Examination of the scale components of a railcar and rail truck show that this instability is an unlikely event that can be eliminated in design.

Figure 2.3 shows the interaction between the radius of curvature and center of gravity (C.G.) of a railcar body. An instantaneous center of rotation (I.C.) exists in which the railcar body and center plate, acting as one rigid body, rotate with the same angular velocity. In the case of the railcar rotating within the concave center bowl insert, the I.C. is constrained to be the radius of curvature for the insert. The interaction of the C.G. of the railcar and the (I.C.) are the determining parameters of the stability of the railcar.

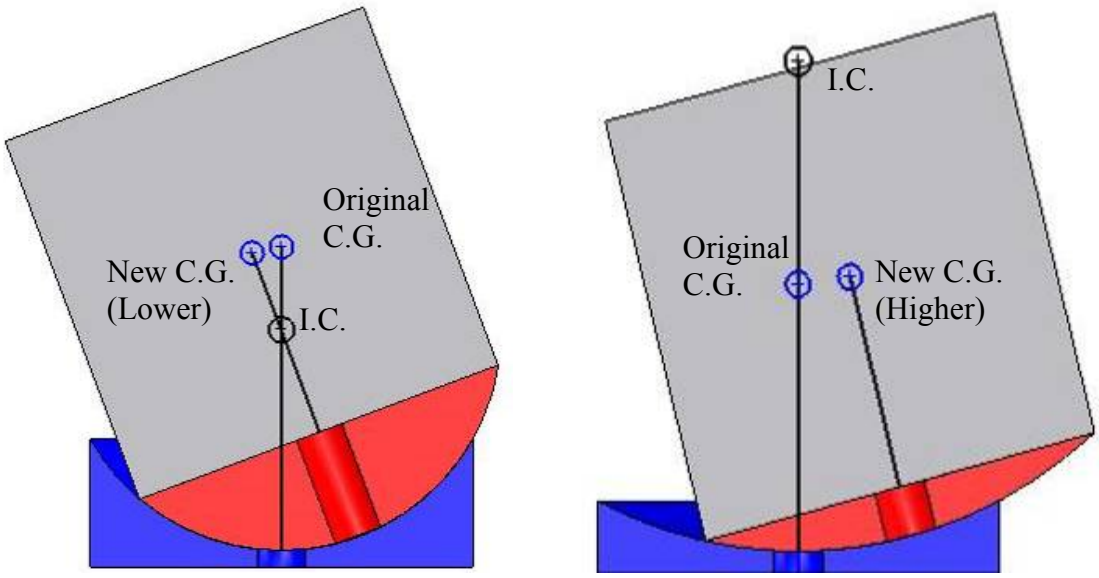

(a) Small Radius of Curvature (b) Large Radius of Curvature

Figure 2.3: Location of Center of Gravity for Small and Large Radii of Curvature

In absence of friction forces, the assembly will right itself if the I.C. (radius of curvature, in this case) of the center plate and railcar body is higher than the C.G. of the railcar body. This is due to the rising of the center of gravity of the car body to create a higher potential energy state, and its tendency to right itself back to its stable position. The railcar weight rights the railcar body to its original (lower) energy state. If the I.C. is below the C.G. of the railcar, the instability of the assembly will increase as the C.G. of the railcar body is lowered and a lower potential energy state is created. The railcar will not return to its original (higher) energy state without external corrective forces. The design radius of curvature is initially chosen as 90 inches (above the center bowl face), which is well above the typical C.G. for a loaded railcar body of 96 inches above the rail or 60 inches above the center bowl face (Hay 1982). A radius of curvature of 90 inches gives a 50% increase in the distance needed for the I.C. to be above the C.G. Such a design will reduce the instances in which stability of the railcar could be compromised, such as eccentric loading or excessive rocking. An alternative

orientation for a spherical set of inserts is one where the bottom insert is convex and the top concave. This orientation is eliminated as it creates an I.C. far below not only the C.G., but even below the track; such an orientation would be highly unstable.

Figure 2.4 shows the spherical bearing assembly drawn to scale for a 16 inch diameter center bowl. The primary difference between the exaggerated drawing and scale drawing is the overlap of the outer wall of the center plate and the inner wall of the center bowl. While in the center position shown in Figure 2.4, the center plate and center bowl inserts are in flush contact and no line contact occurs. The diameter of the standard 16 inch center plate has been modified in the Figure 2.4 to allow for rotation within the center bowl.

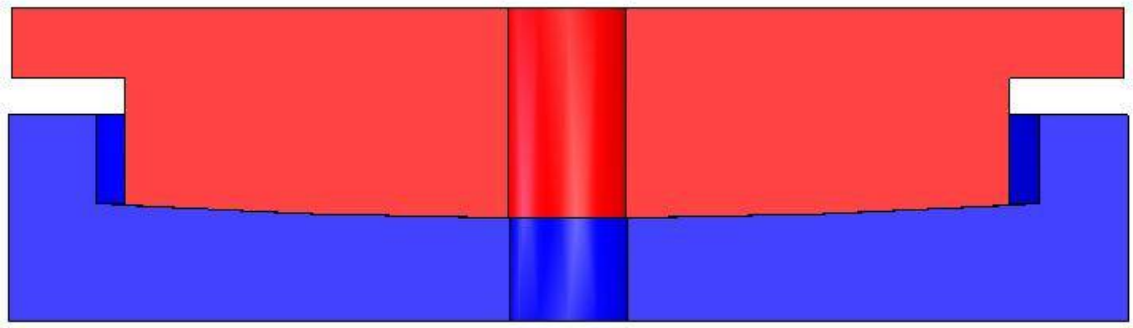

Figure 2.4: Scale Spherical Bearing Interface

In order to achieve constant flush contact between the center plate insert and center bowl insert as the railcar rotates about the I.C., relationships between side bearing gaps, the radius of curvature, and clearances between the top insert and inner center bowl wall must be established. Figure 2.5 shows the pertinent measurements and variables required.

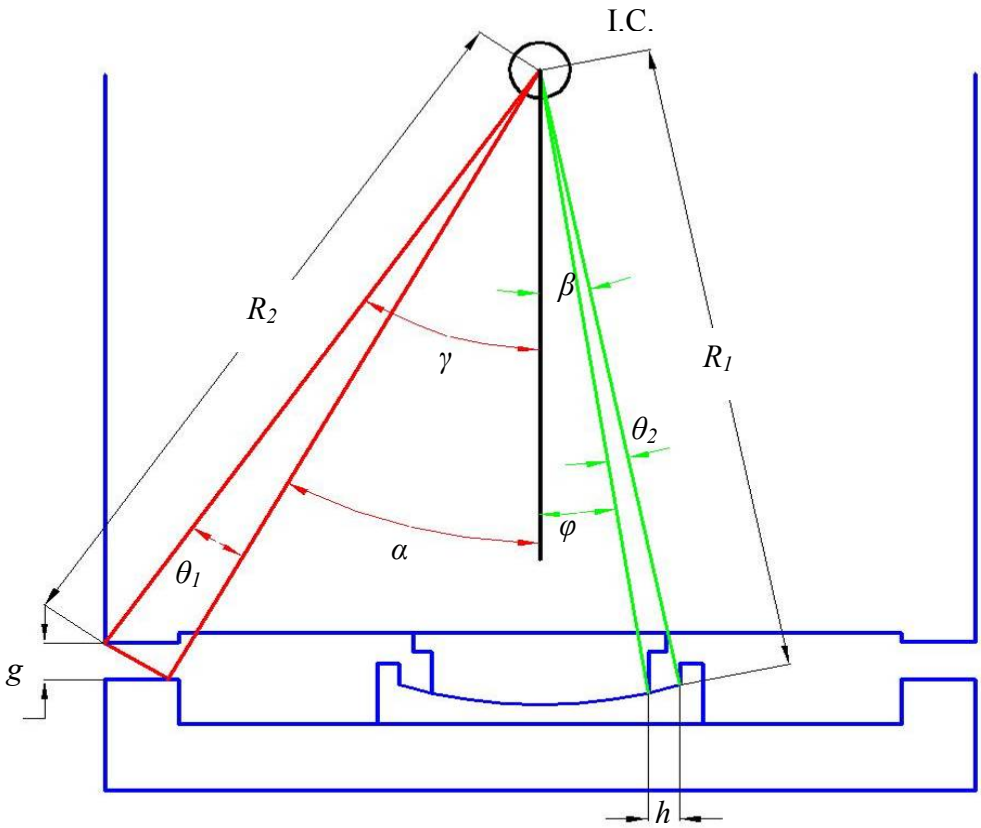

Figure 2.5: Rotation Constraint Relationships

Assuring flush contact at the bearing interface requires that the amount of rotation of the railcar body required for the side bearings to come in contact on either side can be accommodated at the center bowl. If the allowable rotation at the bearing interface is smaller than the required rotation for side bearing contact, the center plate insert would contact the center bowl rim and could bind or even climb the wall. With the railcar geometry fully defined, expressions relating the side bearing gap distance (g), total rotation of the railcar (θ_1), and the horizontal travel of the center plate at the center bowl edge (h) have been determined as follows. The initial geometry of the railcar and truck establish the initial angles γ and β in Figure 2.5.

The following variables are known at the onset of the derivation and are shown in Figure 2.6:

R_1	Radius of curvature at the bearing interface
g	Vertical side bearing gap
d	Diameter of center bowl
t_i	Mid thickness of the center bowl insert
b_1	Side bearing height
a	Horizontal distance from center bowl center to center of side bearing

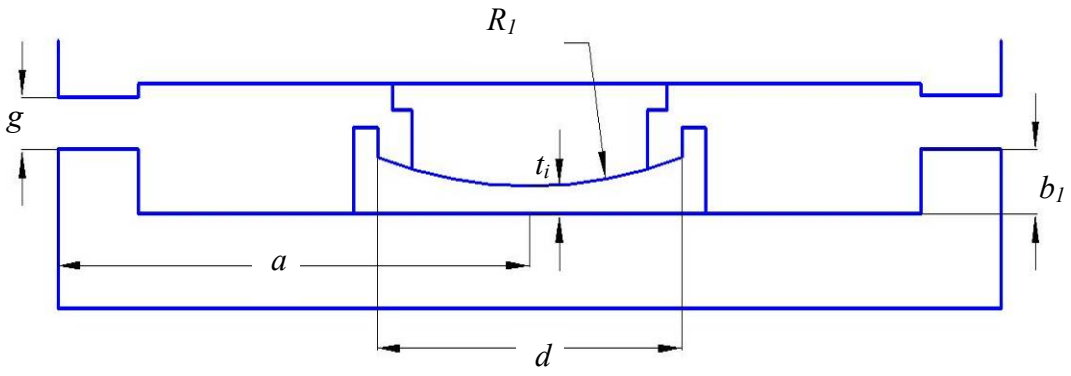

Figure 2.6: Initial Railcar Geometry

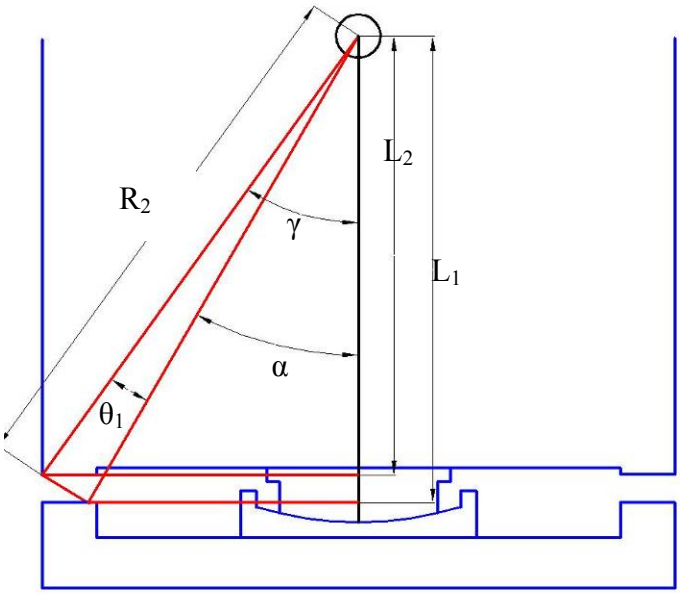

Figure 2.7: Side Bearing Gap Geometry

From Figure 2.6 and 2.7 the angle γ can be calculated from the initial geometric variables as follows

$$\gamma = \tan^{-1}\left(\frac{a}{L_2}\right), \tag{2.1}$$

where

$$L_2 = R_1 + t_i - (b_1 + g). \tag{2.2}$$

With γ known, the radial distance from the I.C. to the upper side bearing is

$$R_2 = \frac{a}{\sin(\gamma)}. \tag{2.3}$$

The vertical gap g can be related to R_2 and the angles shown in Figure 2.7 as follows

$$g = L_1 - L_2 , \tag{2.4}$$

where

$$L_1 = R_2 \cos(\alpha) \tag{2.5}$$

$$\alpha = \gamma - \theta_1 . \tag{2.6}$$

Combining these variables gives the rotation of the railcar body required to close the side bearing gap, *g*, as

$$g = \left(R_2 \cos(\gamma - \theta_1)\right) - \left(R_1 + t_i - (b_1 + g)\right) \tag{2.7}$$

$$\frac{\left(R_1 + t_i - b_1\right)}{R_2} = \cos\left(\gamma - \theta_1\right). \tag{2.8}$$

Solving for θ_1 yields

$$\theta_1 = \gamma - \cos^{-1}\left(\frac{\left(R_1 + t_i - b_1\right)}{R_2}\right). \tag{2.9}$$

Now the center bowl geometry in Figure 2.8 can be used to determine the horizontal travel required by the center plate along the center bowl.

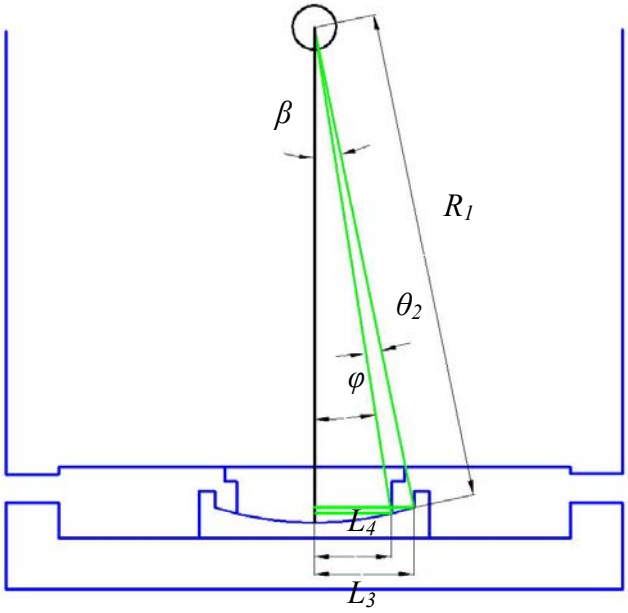

Figure 2.8: Center Plate Horizontal Travel Geometry

The angle β can be calculated from the initial geometry by noting that the center plate will stop rotation along the face after it contacts the side of the center bowl rim.

$$\beta = \sin^{-1}\left(\frac{L_3}{R_1}\right). \tag{2.10}$$

Now, the horizontal travel of the center plate (h) can be related to R_1, β, and θ_2.

$$h = L_3 - L_4, \tag{2.11}$$

where

$$L_3 = \frac{d}{2} \tag{2.12}$$

$$L_4 = R_1 \sin(\varphi) \tag{2.13}$$

$$\varphi = \beta - \theta_2 . \tag{2.14}$$

Combining the above equations, h is:

$$h = \frac{d}{2} - R_1 \sin(\beta - \theta_2) . \tag{2.15}$$

To find the value of h corresponding to the closing of the side bearing gap g, θ_1 and θ_2 are equated and h becomes:

$$h = \frac{d}{2} - R_1 \sin(\beta - \theta_1) . \tag{2.16}$$

The following numerical example illustrates railcar geometry and typical values for horizontal center plate travel (Wolf 2005b, Tournay et al. 2006). The geometry as defined in Figure 2.5 is as follows:

R_1	90 inches
g	1/16 inches
d	16 inches
t_i	0.25 inches
b_1	4.5 inches
a	26 inches

The angle γ and radius R_2 are:

$$\gamma = \tan^{-1}\left(\frac{26\,\text{in}}{90\text{in} + 0.25\text{in} - (4.5\text{in} + 1/16\text{in})}\right) = 16.879 \text{ deg} \tag{2.17}$$

$$R_2 = \frac{26\text{in}}{\sin(16.88\,\text{deg})} = 89.547\,\text{in} \tag{2.18}$$

The rotation of the railcar body is

$$\theta_1 = 16.88\,\text{deg} - \cos^{-1}\left(\frac{(90\text{in} + 0.25\text{in} - 4.5\text{in})}{89.547\text{in}}\right) = 0.138\,\text{deg}. \tag{2.19}$$

The angle β for this set up is:

$$\beta = \sin^{-1}\left(\frac{8}{90}\right) = 5.10\ \text{deg}. \tag{2.20}$$

Finally, the horizontal travel of the center plate, h, is given by

$$h = 8\text{in} - 90\text{in}\ \sin(5.1\,\text{deg} - 0.138\,\text{deg}) = 0.22\,\text{in}. \tag{2.21}$$

The horizontal gap between the center plate and center bowl rim required for flush contact at the bearing interface is approximately 1/4 inches for a radius of curvature of 90 inches and a side bearing gap of 1/16 inches. A comparison of the example to results for such a calculation changing only the side bearing gap to 1/8 inches and 1/4 inches is shown below in Table 2.1.

Table 2.1: Rotation and Center Plate Travel for Various Side Bearing Gaps

	g = 1/16 inches	g = 1/8 inches	g = 1/4 inches
γ (degrees)	16.88	16.89	16.91
R_2 (inches)	89.55	89.49	89.37
θ_1 (degrees)	0.138	0.278	0.560
h (inches)	0.22	0.43	0.88

The equations and results above have been derived for any magnitude of value for θ_1 or θ_2. In reality, these angles are very small and noting that the numerical outcomes for the angle θ_1 are between 0.138 and 0.560 degrees, the expressions for both θ_1 and h can be simplified by including the following small angle approximations

$$\sin\theta \approx \theta\,, \tag{2.22}$$

$$\cos\theta \approx 1\,. \tag{2.23}$$

Implementing these approximations, the derivations for θ_1 and h are shown below. Referring to Figure 2.6 and Equation (2.4), the expression for g in terms of R_2 and the associated angles is

$$g = L_1 - L_2 \tag{2.4}$$

$$g = R_2\cos\alpha - R_2\cos\gamma \tag{2.24}$$

$$g = R_2\big(\cos(\gamma-\theta_1) - \cos(\gamma)\big) \tag{2.25}$$

$$g = R_2\big(\cos(\gamma)\cos(\theta_1) + \sin(\gamma)\sin(\theta_1) - \cos(\gamma)\big)\,. \tag{2.26}$$

Using the small angle approximations,

$$g = R_2\big(\cos(\gamma) + \theta_1\sin(\gamma) - \cos(\gamma)\big), \tag{2.27}$$

and recalling equation 2.3, θ_1 (in radians) is

$$\theta_1 = \frac{g}{a}\,. \tag{2.28}$$

Solving for *h* from Figure 2.7 and Equation (2.11),

$$h = \frac{d}{2} - R_1 \sin\varphi \tag{2.29}$$

$$h = \frac{d}{2} - R_1 \sin(\beta - \theta_2) \tag{2.30}$$

$$h = \frac{d}{2} - R_1\left(\sin(\beta)\cos(\theta_2) - \cos(\beta)\sin(\theta_2)\right). \tag{2.31}$$

Employing the small angle approximations once more,

$$h = \frac{d}{2} - R_1\left(\sin(\beta) - \theta_2\cos(\beta)\right), \tag{2.32}$$

where

$$R_1 \sin(\beta) = \frac{d}{2} \tag{2.33}$$

$$\cos(\beta) = \sqrt{R_1{}^2 - \frac{d^2}{4}}\,. \tag{2.34}$$

Substituting into the equation for *h* and equating θ_1 and θ_2

$$h = R_1\sqrt{1 - \frac{d^2}{4R_1{}^2}} * \frac{g}{a}\,. \tag{2.35}$$

Approximate values for θ_1 and *h* using the previous numerical input are shown in Table 2.2.

Table 2.2: Approximate Rotation and Center Plate Travel
for Various Side Bearing Gaps

	g = 1/16 inches	g = 1/8 inches	g = 1/4 inches
θ_1 (degrees)	0.138	0.275	0.551
h (inches)	0.22	0.43	0.86

With the acceptance and increasing use of constant contact or reduced gap hard contact side bearings, less rotation of the railcar occurs and the required horizontal travel of the center plate within the center bowl is significantly reduced. The implementation of a spherical bearing interface where the center plate and center bowl remain in flush contact throughout the rotation required for side bearing contact reduces the edge contact responsible for component wear.

2.3 Investigation of Conical Interface Geometry

An investigation into alternative interface geometries revealed a conical interface as a possible improvement over flat plate contact. In such a layout, a shallow conical interface would work to center the center plate in the center bowl. Figure 2.9 shows a conical interface layout in both the centered and tilted positions. In contrast to the spherical bearing interface, a conical interface has several locations where line or edge contact could occur. Also in contrast to a spherical geometry, the movement of the center plate within the center bowl would be less of a smooth rotation and more of a jerking, start-stop motion.

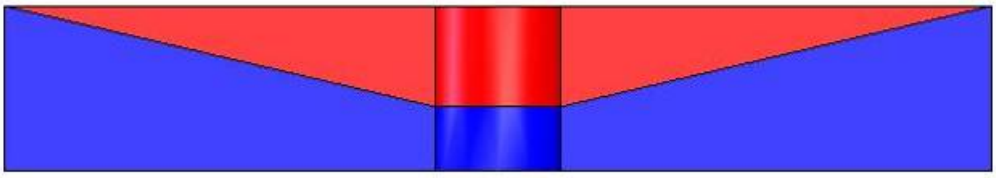

(a) Centered Position

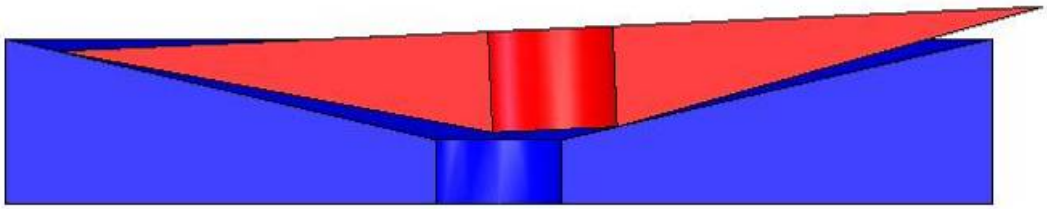

(b) Tilted Position

Figure 2.9: Exaggerated Conical Bearing Interface

For example, in Figure 2.9(b) the right tip of the center plate insert will gouge into the upper face of the center bowl insert. This is an extreme case of point or line loading that would occur any time the center plate rocked within the center bowl, much like flat plate contact.

2.4 Geometry Dimensions

Considering the models and discussion above, a spherical bearing interface is chosen for the preliminary geometry layout. Figure 2.10 shows the preliminary dimensions of such a spherical interface with a 16 inch diameter center bowl.

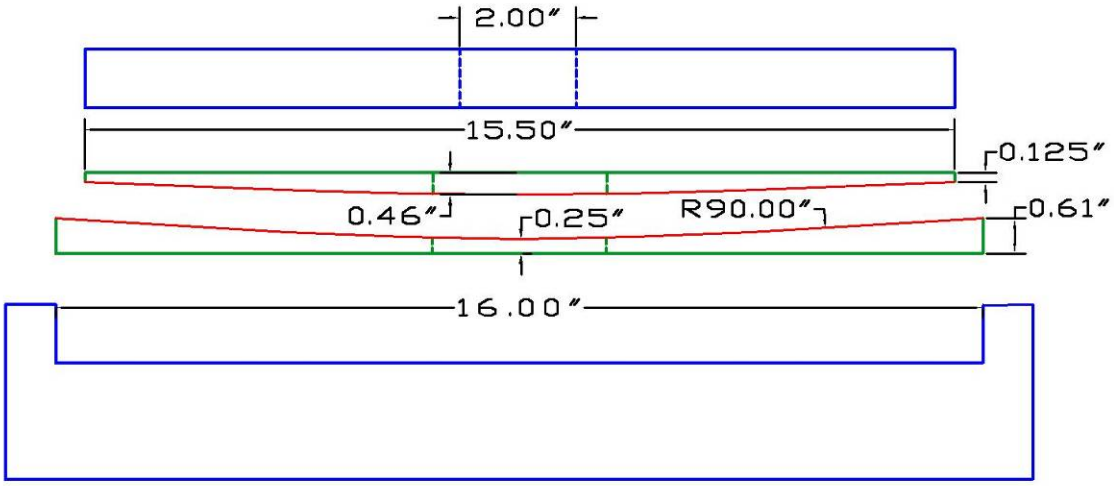

Figure 2.10: Design Geometry

The geometry shown in Figure 2.10 was calculated so that a reasonable amount of steel material exists at both the center of the bottom insert and the outer edges of the upper insert. The total increase in height for a railcar with these inserts is 0.71 inches. The bottom insert has an outer thickness of 0.61 inches and an inner thickness of 0.25 inches, which results in a required radius of curvature of approximately 90 inches. Consequently, the thickness at the center of the center plate insert is 0.46 inches. The inner diameter of both of the inserts is 3 inches which will allow for the small rotations of the center plate within the center bowl.

Railcars can be retrofitted to accommodate existing railcar stock. The lower insert can be simply dropped into an existing center bowl, while the upper insert can be welded to the existing center plate. With the use of existing plastic center bowl liners, the railcar must be raised off of its trucks and inspected on a regular basis. With this proposed design, railcar owners will not only have less physical equipment costs from liners and lubrication, but hauling schedules may be able to run longer without maintenance stops.

2.5 Dynamic Investigation

With the kinematics of the railcar/rail truck interface examined and the design geometry completed, an investigation of the dynamic interaction between the railcar and rail truck was performed. Specifically, the interaction of the interface was examined to determine the possibility of a dynamic instability due to oscillatory motion within the center bowl. Such an instability caused by dynamic amplification can occur in harmonic systems when the system is driven at the system's natural frequency of vibration. Damping, or energy loss, can serve to mitigate, or even eliminate this resonant behavior. Given the broad spectrum of frequencies to which the railcar is subjected as it traverses track, a dynamic analysis is needed to produce both the natural frequency of the system as well as the damping ratio caused by friction.

The first step in determining the natural frequency and damping ratio of the system is the construction of the equation of motion (EOM). In general, a body has six degrees of freedom (DOF's) that correspond to translation in the x, y, and z coordinates and rotation about each of the x, y, and z axes. Figure 2.11 shows the above coordinates and their corresponding directions in relation to the rail truck.

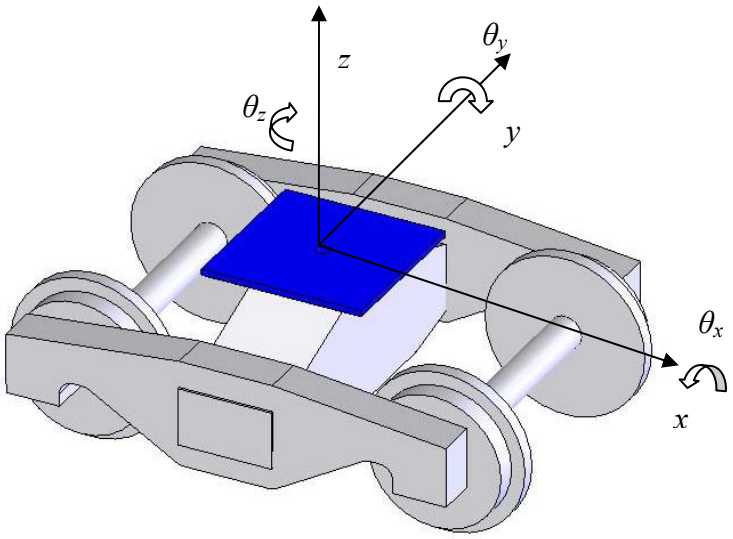

Figure 2.11: Coordinate System

Because the bearing interface is spherical, translational DOF's are assumed to be fixed; only rotational motion can occur at the interface. Taking the railcar and truck to be rigid bodies eliminates truck warping and car body bending which corresponds to rotation about the *y* and *z* axes, respectively. The above assumptions leave rotation about the *x* axis as the only DOF for the dynamic analysis. As mentioned earlier in the chapter, the car body rotates within the center bowls through the angle θ_x (θ from the preceding sections) about the I. C. Beginning with the assumption of a frictionless interface, the free body diagram (FBD) of the system rotated through an angle θ are shown in Figure 2.12.

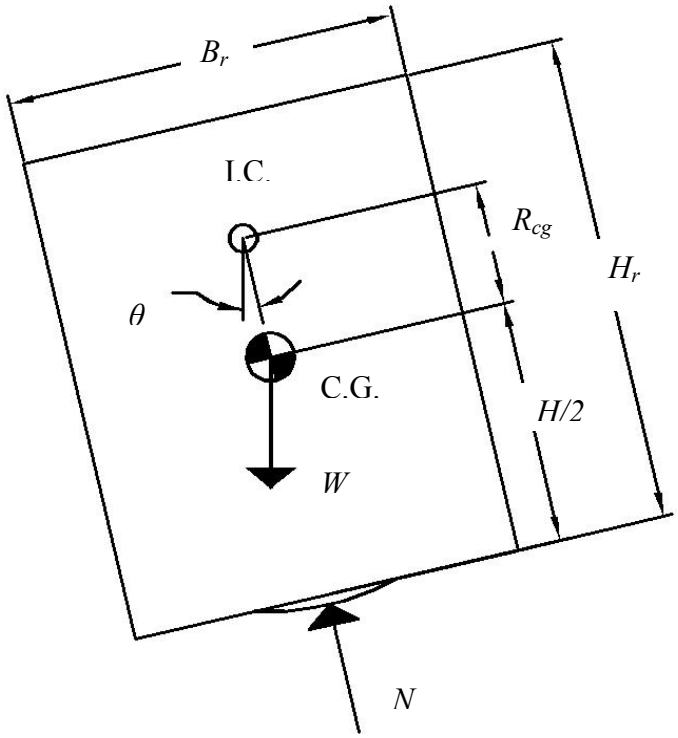

Figure 2.12: Free Body Diagram

Construction of the EOM from Figure 2.12 requires the summation of moments about the I.C. and gives:

$$\sum M_{I.C.} \circlearrowleft = J\ddot{\theta} \tag{2.36}$$

$$J\ddot{\theta} = -WR_{cg} \sin\theta \tag{2.37}$$

The mass moment of inertia with respect to the I.C. of the railcar body is represented by *J*. Rearranging and using the small angle approximation from Equation (2.22)

$$\ddot{\theta} + \frac{WR_{cg}}{J}\theta = 0 \quad . \tag{2.38}$$

The natural frequency of a harmonic equation of this form is the square root of the theta coefficient

$$\omega = \sqrt{\frac{WR_{cg}}{J}} \quad . \tag{2.39}$$

The inclusion of friction into the EOM from Equation (2.38) is shown below and consists of a moment caused by a friction traction over the surface area of the bearing interface which opposes the direction of the angular velocity

$$\ddot{\theta} + \frac{WR_{cg}}{J}\theta + \frac{M_f}{J}\text{sgn}[\dot{\theta}] = 0 \quad . \tag{2.40}$$

Appendix A.1 illustrates the derivation of M_f and gives the approximate result

$$M_f = \mu R_1 W \ . \tag{2.41}$$

Equation (2.40) now becomes

$$\ddot{\theta} + \frac{WR_{cg}}{J}\theta + \frac{\mu R_1 W}{J}\text{sgn}[\dot{\theta}] = 0 \ . \tag{2.42}$$

This equation is nonlinear because of the sign change required by the frictional term. In order to discover the amount of damping provided by the friction, an equivalent linear EOM is needed, and has the following form.

$$\ddot{\theta} + \frac{c_{eq}}{J}\dot{\theta} + \frac{WR_{cg}}{J}\theta = 0 \tag{2.43}$$

The value of c_{eq} is determined by equating the average rate of energy dissipated by the friction moment in Equation (2.44) and the viscous damping in Equation (2.43). Noting from dynamics that the rate of energy dissipated is the damping moment multiplied by the angular velocity, the following relationship between c_{eq} and M_f can be made (Chopra 2001).

$$\left\langle M_f \ \text{sgn}[\dot{\theta}]\dot{\theta} \right\rangle = \left\langle c_{eq}\dot{\theta}^2 \right\rangle . \tag{2.44}$$

The notation $\langle\ \rangle$ represents the time average of the expression inside. This equation can be further simplified to the following

$$\left\langle M_f \left|\dot{\theta}\right|\right\rangle = \left\langle c_{eq}\dot{\theta}^2 \right\rangle, \tag{2.45}$$

and rearranging,

$$c_{eq} = \frac{M_f \left\langle \left|\dot{\theta}\right| \right\rangle}{\left\langle \dot{\theta}^2 \right\rangle}. \tag{2.46}$$

Assuming that the solution to the EOM is harmonic and of the form in Equation (2.47), the time average required in Equation (2.46) can be taken over half a cycle with θ ranging from θ_0 to θ_f and time ranging from zero to the time required by Equation (2.47)

$$\theta(t) = \theta_0 \cos(\omega t). \tag{2.47}$$

Taking θ_0 to be $-\theta_1$ and θ_f to be $+\theta_1$ in Equation (2.47), Equation (2.48) is solved for t_f

$$\theta_1 = -\theta_1 \cos(\omega t_f) \tag{2.48}$$

$$t_f = \frac{\pi}{\omega}. \tag{2.49}$$

Noting that the time average of a function is the integral of the function over the time interval divided by the time interval (Stewart 1999), Equation (2.46) can now be written as

$$c_{eq} = \frac{M_f \dfrac{1}{t_f}\displaystyle\int_0^{t_f} \left|-\theta_0 \omega \sin(\omega t)\right| dt}{\dfrac{1}{t_f}\displaystyle\int_0^{t_f} (-\theta_0 \omega \sin(\omega t))^2 \, dt} \tag{2.50}$$

$$c_{eq} = \frac{(\mu R_1 W)(2\theta_1)}{\dfrac{\pi \omega \theta_1^{\,2}}{2}} = \frac{4\mu R_1 W}{\pi \omega \theta_1} \tag{2.51}$$

For an EOM of the form in Equation (2.43), the critical damping and damping ratio are defined (Chopra 2001) as

$$c_{cr} = 2J\omega \tag{2.52}$$

$$\zeta = \frac{c_{eq}}{c_{cr}}, \tag{2.53}$$

and substituting values of c_{eq} and c_{cr},

$$\zeta = \frac{\frac{4\mu R_1 W}{\pi\omega\theta_1}}{2J\omega} = \frac{2\mu R_1 W}{\pi\omega^2\theta_1 J}. \tag{2.54}$$

As an estimate on typical natural frequency and damping ratio values for a railcar with a spherical bearing interface, the follow values are applied to the above equations:

W = 286,000 pounds

H_r = 10 feet

B_r = 8 feet

R_{cg}= 2.5 feet

μ= 0.3

θ_1= 0.00241 radians

R_1= 7.5 feet

The mass moment of inertia for the railcar about the I.C. is

$$J = \frac{286{,}000\ \text{lbs}}{32.2\,\text{ft/s}^2}\left(2.5\,\text{ft}^2 + \frac{8\,\text{ft}^2 + 10\,\text{ft}^2}{12}\right) = 1.77\times10^5\ \text{slug}-\text{ft}^2. \tag{2.55}$$

The natural frequency of the dynamic system is

$$\omega = \sqrt{\frac{286{,}000\ \text{lbs} * 2.5\,\text{ft}}{1.77\times10^5\ \text{slug}-\text{ft}^2}} = 2.01\,\text{rad/s}. \tag{2.56}$$

The damping ratio of the system is

$$\zeta = \frac{2 * 0.3 * 7.5\,\text{ft} * 286{,}000\,\text{lbs}}{\pi(2.01\,\text{rad/s})^2 * 0.0024\,\text{rad} * 1.77\times10^5\ \text{slug}-\text{ft}^2} = 240.1. \tag{2.57}$$

A damping ratio of more than unity implies that the system is overdamped and the oscillatory motion will not occur. Thus, dynamic effects will not cause any detrimental resonant motion in the center bowl (Chopra 2001).

CHAPTER III

MATERIAL TESTING PROCEDURES

3.1 Protective Material

The center bowl/center plate inserts can be coated with a material that gives both excellent wear resistance and a favorable friction coefficient. While silicon nitride or silicon carbide may have ideal ceramic properties for this application, the process of depositing these ceramics onto steel substrates with large surface areas is problematic. In attempts to coat silicon nitride onto steel via plasma deposition, the plasma deposition equipment was unable to heat the silicon nitride to an appropriate deposition temperature.

An alternative to ceramic coating is a metallic based protective coating. Tungsten carbide and chrome nickel have excellent wear and hardness properties and are readily coated to steel. For this reason, tungsten carbide and chrome nickel were tested in the High Bay Structural and Materials Testing Laboratory at Texas A&M University. Material compositions of both materials are shown below in Table 3.1 and Table 3.2.

Table 3.1: Material Composition of Tungsten Carbide Cobalt Chrome Coating

Tungsten Carbide Cobalt Chrome	
Material	% Composition
Tungsten Carbide (WC)	86
Cobalt (Co)	10
Chrome (Cr)	4

Table 3.2: Material Composition of Ferro Chrome Nickel Coating

Ferro Chrome Nickel	
Material	% Composition
Iron (Fe)	27.8
Chrome (Cr)	31
Nickel (Ni)	28.5
Silicon (Si)	1.5
Boron (B)	4
Copper (Cu)	3.2
Molybdenum (Mo)	4

Cobalt is present in many tungsten carbides as a metallic element that provides a matrix or binder for the primary elements. Small amounts of chrome are used to reduce corrosion and oxidation as well as increasing the maximum service temperature. Chrome nickel has many more alloying elements seen in Table 3.2. Its high percentage of both chrome and nickel help reduce corrosion. Boron and molybdenum are added for increased strength and hardness.

As assured in specifications obtained from Hitemco Southwest, the tungsten carbide material has a Rockwell 'C' Scale hardness of at least 63, or about 7 on the Mohs Hardness Scale (Lide 2005). Variation of material hardness is attributed to the different alloying materials used. In this case, the use of cobalt and chrome can slightly decrease the hardness. Typical values of hardness for pure tungsten carbide are 8-9 on the Mohs Hardness scale (Lide 2005). The chrome nickel material is softer with a Rockwell 'C' Hardness of 40-45 corresponding to a Mohs Hardness of 6-7 (Callister 2003).

3.2 Test Setup

In order to investigate the effects of a protective coating on the center bowl/ center plate bearing surface, a series of reduced scale laboratory tests was performed to

estimate the unlubricated friction coefficients for varying materials on both steel and tungsten carbide. Wear of each combination of materials was also documented. The matrix in Table 3.3 below shows the combination of materials tested and how many tests were performed for each combination.

Table 3.3: Specimen Material Combinations Used in Laboratory Testing

		Specimen Material		
		Steel	Tungsten Carbide	Chrome Nickel
Base "Pestle" Material	Steel	1	4	3
	Tungsten Carbide	1	3	3

The "mortar and pestle" test assembly in Figure 3.1 was fabricated to test coated tablets in an axial-torsional load frame. The top ("pestle") and bottom ("mortar") pieces both fit into the load frame and the coated steel discs were held in place and centered by 3 set screws on the top rim of the mortar. This setup allowed for a rapid interchange of specimens between testing. The load frame applied axial force through the pestle while the mortar and disc were rotated through an angle of twist at a constant rate. Figure 3.1(c) shows the interaction between the pestle and mortar, and Figure 3.1(d) shows the altered pestle in which tungsten carbide coated specimen #3 was welded to the pestle. To ensure that the surface coating of tungsten carbide was unaffected by the heat of the welding procedure, the pestle was ground at the edges so a groove weld could be formed. This reduced the heat from the weld from altering the surface of specimen #3.

(a) Specimen and Mortar

(b) Specimen Fixed to Mortar

(c) Pestle and Mortar Interface

(d) Modified Pestle

Figure 3.1: Test Apparatus

An axial-torsional load frame was used to determine torque as a function of rotation experienced by test specimens for each surface. The energy from torque vs. rotation hysteresis loops was equated to the work done by the friction force on the specimen surface. Controlled parameters (axial load, angle of twist, twist rate, and test duration) were used to calculate friction coefficients between steel and various protective materials. Appendix A.2 shows the derivation of the relationships between the hysteresis energy and the controlled parameters. The resulting equation from Appendix A.2 is

$$\mu = \frac{3E_L}{4P_T R_a \theta_{z\max}}. \tag{A.28}$$

Steel tablets were machined and coated with the metallic based materials according to Table 3.4. Each 2 inch diameter, 0.5 inch thick tablet was made of 4140 steel which was coated with an approximately 0.020 inch protective coating. One disc was left uncoated to serve as a control to confirm accurate friction coefficient results for steel on steel contact. The control also served as a benchmark on which to compare material wear.

Table 3.4: Specimen Coatings

Specimen #	Coating Material
1	Tungsten Carbide
2	Tungsten Carbide
3	Tungsten Carbide
4	Tungsten Carbide
5	Chrome Nickel
6	Chrome Nickel
7	Chrome Nickel
12	None

3.3 Test Parameters

The axial load used in the laboratory tests was that which creates a typical state of stress found in a center bowl/center plate bearing interface. A heavily loaded railcar weighs approximately 286 kips. Field tests have shown that four side bearings on the railcar (two per truck) can typically take about 10% of the total load at any time (Tournay et al. 2006). The remaining load transferred through each center plate into each center bowl is

$$P_s = \frac{286\,\text{kips} - 0.10 \times 286\,\text{kips}}{2} = 128.7\ \text{kips}. \tag{3.1}$$

The stress in the center bowl was found by dividing P_s by the area of the center bowl. Assuming a 16 inch diameter center bowl with a 2 inch hole for the center pin, the stress is

$$\sigma_B = \frac{128.7\,\text{kips}}{\pi\left(8\,\text{in}^2 - 1\,\text{in}^2\right)} = 0.65\ \text{ksi}. \tag{3.2}$$

In order to achieve the same state of compressive full scale stress for a 2 inch diameter specimen, a smaller force (P_T) was applied

$$P_T = 0.65\,\text{ksi} \times \pi\,\text{in}^2 = 2.04\ \text{kips} \cong 2\ \text{kips}. \tag{3.3}$$

Unlike the axial force which was scaled down for test specimen dimensions, the angle of twist needed for laboratory tests is identical to the twisting of the center plate against the center bowl that occurs in the field. A degree of curvature (*D*) of 6° for a 100 foot chord (*C*) is the maximum safe curvature for a horizontal curve in railroad engineering (Wolf and Ghilani 2006). This is approximately the same angle used in tests for determining issues with truck component performance (Tournay et al. 2006). This angle was used with a proper geometric setup to produce the maximum angle of twist

(θ_{zmax}) between the center bowl and center plate throughout a series of horizontal curves. In railroad engineering, horizontal curves are defined by 100 foot chord lengths as shown in Figure 3.2 (Wolf and Ghilani 2006).

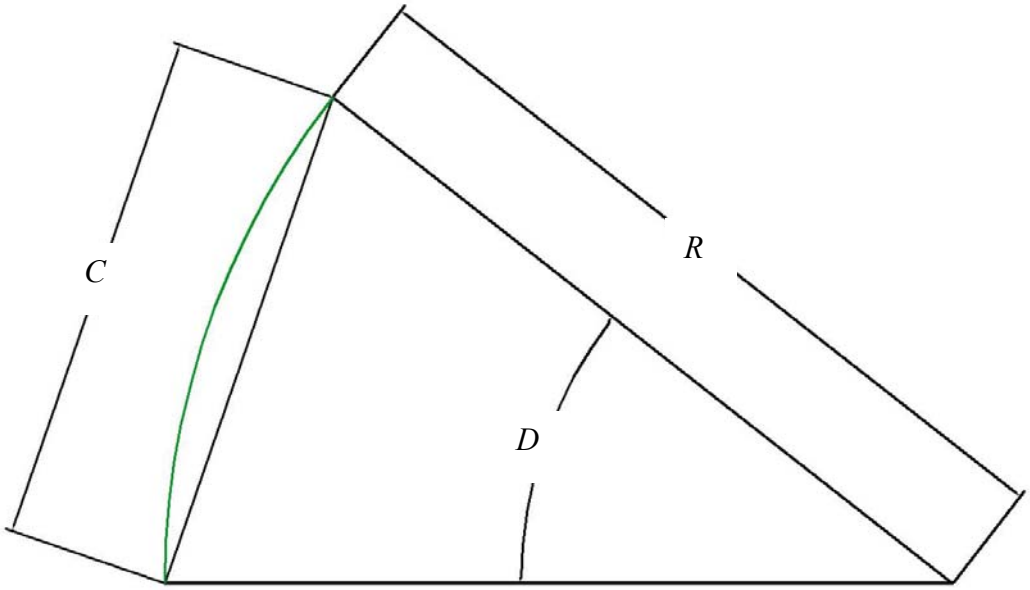

Figure 3.2: Standard Rail Curvature

The following relationship was obtained from Figure 2.4

$$\sin\tfrac{1}{2}D = \frac{\frac{1}{2}C}{R}. \tag{3.4}$$

The radius of curvature (R), to the centerline of the rail, for this configuration is

$$R = \frac{\frac{1}{2}C}{\sin\frac{1}{2}D} = \frac{50\,\text{ft}}{\sin 3\,\text{deg}} = 955.4\,\text{ft}. \tag{3.5}$$

Figure 3.3 shows the portion of the curve in Figure 3.2 for a standard railcar length which now encompasses a smaller central angle (D'). The geometry was adjusted by altering the chord length to a standard railcar length of 40 feet (C') while keeping the same radius of curvature (Hay 1982).

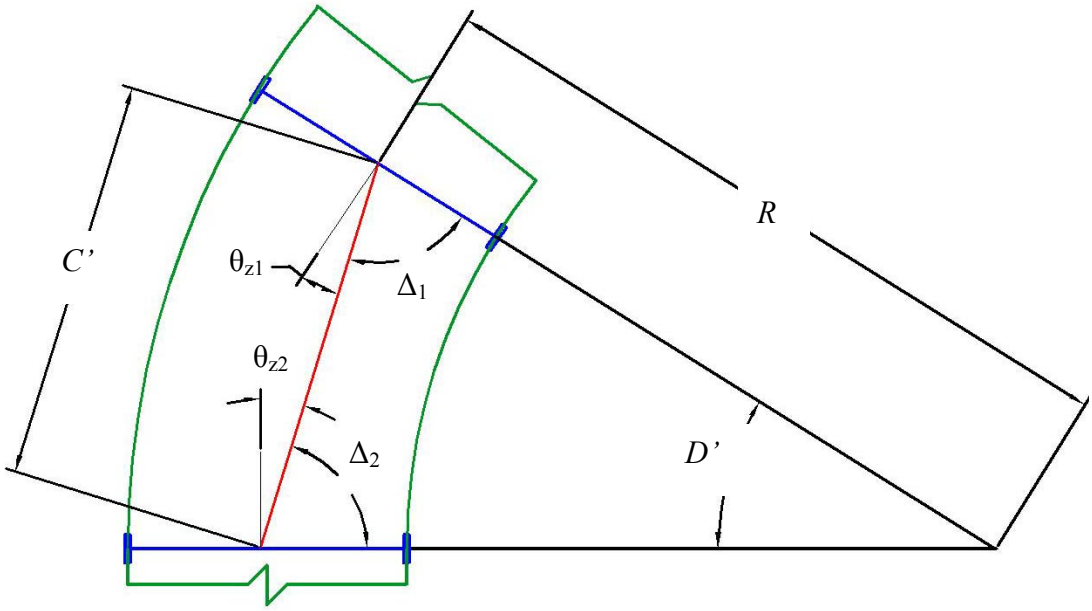

Figure 3.3: Rail Curvature between Truck Centers

The new central angle is:

$$D' = 2\sin^{-1}\left(\frac{\frac{1}{2}C'}{R}\right) = 2\sin^{-1}\left(\frac{\frac{1}{2}\,40\,\text{ft}}{955.4\,\text{ft}}\right) = 2.40^{\circ} \qquad (3.6)$$

The central angle (D') was then used to determine the angles of twist φ_1 and φ_2. The triangle in Figure 3.3 defined by the radii of the curve (to the centerline of the rails) and the center-to-center truck length is isosceles. Thus, the angles Δ_1 and Δ_2 are equal and thus θ_{z1} and θ_{z2} are equal. Dropping the subscripts and using Δ and θ_z, the following relationships were used to relate θ_z to the know quantity D'

$$\Delta + \theta_z = 90 \deg \tag{3.7}$$

$$2\Delta + D' = 180 \deg . \tag{3.8}$$

Combining Equations (3.6a) and (3.6b)

$$\theta_z = \frac{D'}{2} = 1.20 \ \deg . \tag{3.9}$$

Knowing θ_z, the total angle of twist that occurs between the center bowl and center plate was determined. Figure 3.4 is a layout of a case in which the twisting of truck components consists of four stages: (1) tangent track entering a curve, (2) a spiral curve to the right, (2) an immediate spiral curve to the left, and (4) tangent track exiting the curve. The center line rail arc lengths of the curves in stages 2 and 3 are not required to be equal because these differences do not cause a change in θ_z. A change in R or a reversal of curvature causes θ_z to change and thus the transition from the second stage to the third stage of Figure 2.6 creates the maximum total angle of twist (θ_{zmax}) between center bowl and center plate for a rail curvature of 6 degrees.

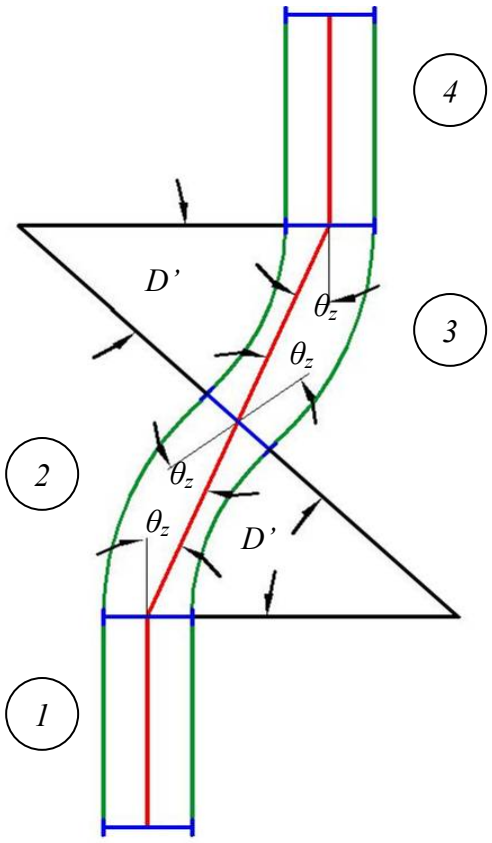

Figure 3.4: Rail Geometry Maximizing Center Bowl Twist

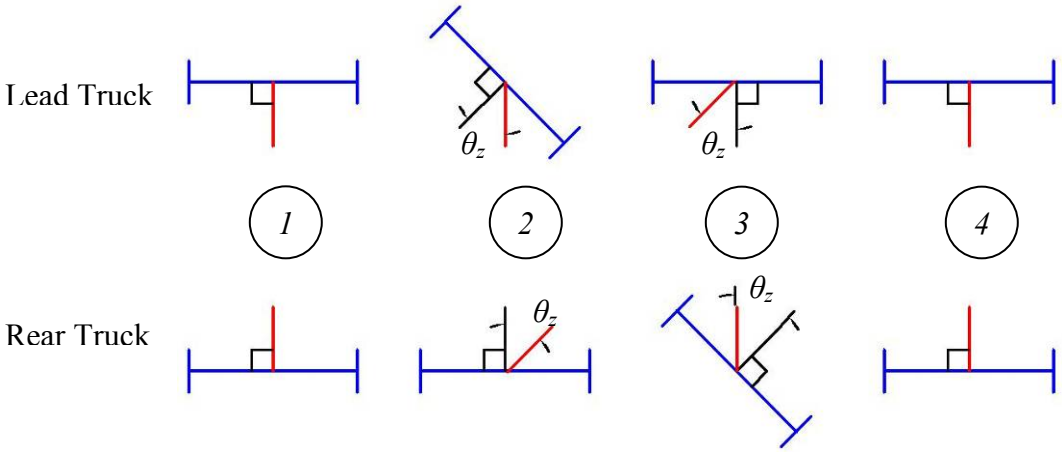

Figure 3.5: Lead and Rear Truck Alignments

As the railcar follows the track, the lead and rear trucks rotate independent of each other, but through the same angle θ_z or $2\theta_z$. Each of these four stages corresponds to a lead and rear truck alignment, as seen in Figure 3.5. The red lines represent the centerlines of the railcar bodies which are either perpendicular to the trucks (Stages 1 and 4) or rotated through the angle θ_z (Stages 2 and 3). Both the lead and rear trucks rotate through the same total angle $\theta_{zmax.}$ For example, the lead truck starts out perpendicular the railcar body centerline (Stage 1), rotates clockwise through θ_z (Stage 2), rotates counterclockwise through $2\theta_z$ (Stage 3), and finally clockwise through θ_z again back to perpendicular (Stage 4). From inspection of this rotation, the total angle of twist was determined

$$\theta_{z\max} = 2\theta_z = 2.40\deg \cong \pm 3\deg . \tag{3.10}$$

3.4 Laboratory Testing

The operational capabilities of the axial-torsional load frame were the primary factors in determining the twist rates for the laboratory tests. Under the given axial load and angle of twist, an appropriate range of operational twist rates was 0.5 – 1.5 Hz. After preliminary tests on specimen #7 with varying twist rates showed no effect on torque vs. time results, a single twist rate of 1.0 Hz was used for all subsequent tests.

Before running tests at the desired 2 kips, a 0.5 kip test run was done to ensure that the axial-torsion load frame (Figure 3.6) could accommodate the torque produced by the test. Subsequent tests were performed at 0.5 kip increments until 2 kips was safely reached. To ensure the proper final torque value from which the friction coefficient could be calculated, the tests were run until peak torque values reached constant magnitude. Each specimen was subjected to 3 individual 30 second tests, which provided enough time to reach constant magnitude torque readings for all specimens. Between tests, the temperature of the contact surface was measured with a thermal gun to ensure that dramatic temperature increases were not occurring on the bearing surface.

Laboratory temperature conditions ranged from 72° F to 76° F, and bearing surface temperatures never changed by more than 2° F.

Before and after testing each specimen, the specimen and pestle were sanded to a 400 grit finish using silicon carbide sandpaper. This procedure helped ensure that each specimen was undergoing a similar initial contact condition.

Figure 3.6: Axial-Torsional Load Frame and Data Acquisition

CHAPTER IV

RESULTS

4.1 Friction Coefficients for the Steel Pestle Tests

Friction coefficient values were obtained using the torque vs. rotation output described in Chapter III. Torque vs. total rotation plots and torque vs. plastic rotation plots were created for all tests and these were used to determine friction coefficients representative of the different materials tested. The MATLAB code for calculating friction coefficients is found in Appendix D.3. Figure 4.1 shows the torque vs. rotation plot for specimen #12 on the steel pestle.

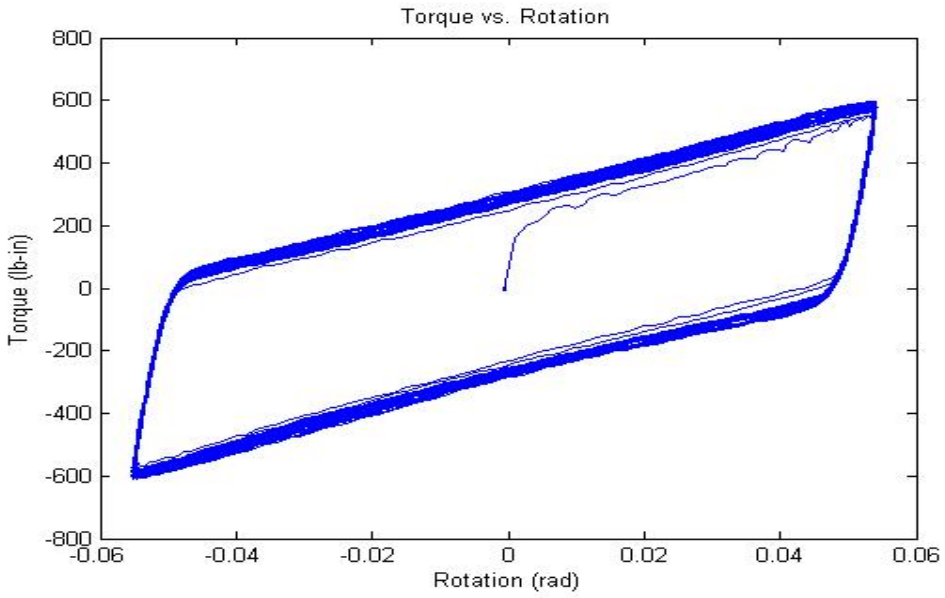

Figure 4.1: Representative Torque vs. Rotation Results for Steel Pestle

All torque and rotation test plots can be found in Appendix B. The test data shows consistent trends in both the tungsten carbide on steel and chrome nickel on steel

contact. Table 4.1 summarizes the results found for all materials tested with the steel pestle.

Table 4.1: Summary of Friction Coefficient Results for Steel Pestle

Specimen No.	μ
1 (WC)	***0.45***
2 (WC)	***0.31***
3 (WC)	***0.28***
4 (WC)	***0.29***
5 (Cr-Ni)	0.74
6 (Cr-Ni)	0.40
7 (Cr-Ni)	0.57
12 (Steel)	***0.41***

The values shown in Table 4.1 represent the friction coefficient calculated by the energy method described in Chapter II, with the lowest values occurring for tungsten carbide shown in bold.

The friction coefficient of steel on steel was found to be 0.41 which agrees with results found in the literature, and is shown in bold in Table 4.1 (Lide 2005). The tungsten carbide results, also shown in bold in Table 4.1, are lower than friction coefficients of steel on steel in all cases except specimen #1. The friction coefficients for chrome nickel on steel range from 0.40-0.74.

4.2 Friction Coefficients for the Tungsten Carbide Pestle Tests

After seeing the damage sustained by the steel pestle during testing, the idea of coating both surfaces of the bearing interface was examined. Friction coefficients between the tungsten carbide pestle and the coated specimens are calculated in the same manner as for the steel pestle tests. Table 4.2 shows the friction coefficient values for the tests on the tungsten carbide pestle.

Table 4.2: Summary of Friction Coefficient Results for Tungsten Carbide Pestle

Specimen No.	μ
1 (WC)	***0.24***
2 (WC)	***0.22***
4 (WC)	***0.12***
5 (Cr-Ni)	0.47
6 (Cr-Ni)	0.12
7 (Cr-Ni)	0.22
12 (Steel)	0.30

The friction coefficient values of the tungsten carbide on steel (specimen #12 on the tungsten carbide pestle) in Table 4.2 for the second set of tests agree with results from Table 4.1 (specimen #3 on the steel pestle). The friction coefficients for tungsten carbide on tungsten carbide (in bold in Table 4.2) are lower than those of tungsten carbide on steel. The values for tungsten carbide on itself range from 0.12-0.24, where as values for chrome nickel on tungsten carbide are scattered from 0.12-0.47.

4.3 Specimen Wear for Steel Pestle Tests

Also important to the success of the design is the ability of the protective coating to withstand the loading conditions found at the bearing interface while minimizing wear. Photographs of each specimen were taken after testing and all presented in Appendix C. Figure 4.2 shows a tungsten carbide coated specimen before and after testing. The light spots in Figure 4.2(b) are areas of localized polishing which was the only damage incurred from the axial-torsional test. Figure 4.3 shows a chrome nickel coated specimen in a similar manner.

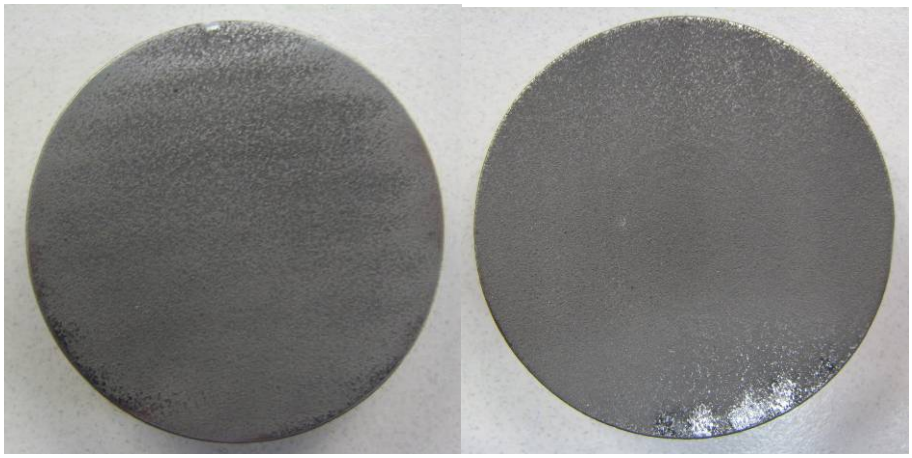

(a) Before Testing (b) After Testing

Figure 4.2: Tungsten Carbide Coated Specimen #3

(a) Before Testing (b) After Testing

Figure 4.3: Chrome Nickel Coated Specimen #6

The black outline of wear on the specimen in Figure 4.3(b) is a powder that appeared on all three chrome nickel coated specimens after testing. The coating on each of the coated specimens was not damaged during the laboratory tests and no visible change in

the depth of the coating or difference in texture occurred. Specimen #7 shown in Figure 4.4 was damaged at the coating facility, and while it showed localized wear and a black powdery substance like the other specimens, no further cracking or chipping of the ceramic coating occurred. The damage to the coating on specimen #7 occurred when the specimen was removed from the rod to which it was welded for plasma deposition of the coating material. Such a process of spraying would not be used for full scale inserts.

Figure 4.4: Specimen #7 Damaged Prior to Testing

A visual inspection of the wear sustained by the steel specimen shows a more severe wear pattern than the coated specimens. Although consistent with the size and shape of the wear on the coated specimens, the steel specimen has significant wear into the thickness of the surface. Figure 4.5 shows the steel specimen before and after testing.

(a) Before Testing (b) After Testing

Figure 4.5: Steel Specimen #12

Figure 4.6 shows a close visual comparison of damage between specimens of each material. While the coated specimens experienced local polishing, the steel specimen's surface underwent pitting and local plastic deformation perceptible by touch.

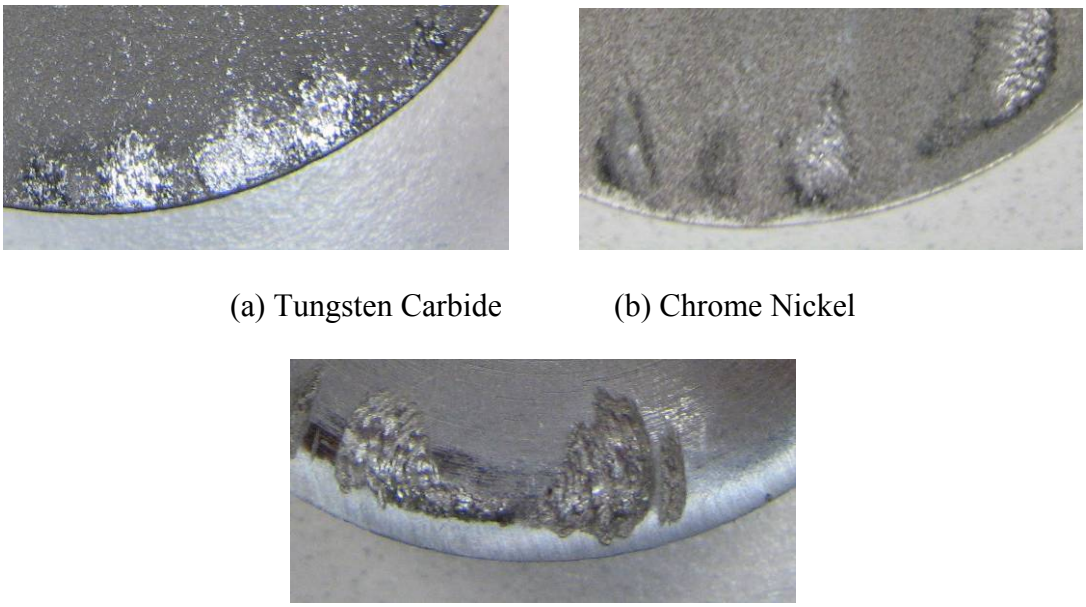

(a) Tungsten Carbide (b) Chrome Nickel

(c) Steel

Figure 4.6: Comparison of Specimen Wear for Steel Pestle Test

The steel pestle sustained significant damage to its surface as well. The surface of the pestle had to be sanded to a 400 grit finish after each test to ensure the damaged caused by the previous test did not affect the subsequent test.

4.4 Specimen Wear for Tungsten Carbide Pestle Tests

Wear on the specimens for the tungsten carbide pestle tests occurred in similar patterns, but was less severe. All wear took place near the outer edge of the specimen as in the previous steel pestle tests. Figure 4.7 again compares the wear of each type of material after 3 tests against the tungsten carbide. When comparing the steel specimen wear against the steel and tungsten carbide pestles, the steel wear against the tungsten carbide is far less severe than steel on steel contact. The tungsten carbide pestle did not wear appreciably throughout any of the tests as the steel pestle did.

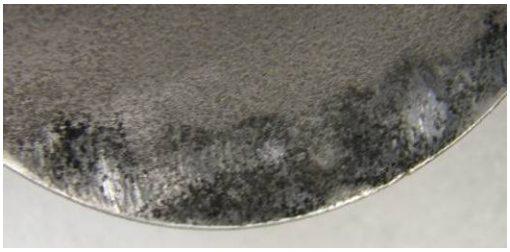

(a) Tungsten Carbide

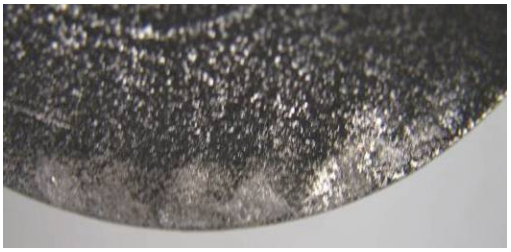

(b) Chrome Nickel

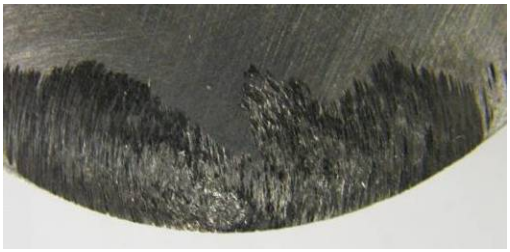

(c) Steel

Figure 4.7: Comparison of Specimen Wear for Tungsten Carbide Pestle Test

CHAPTER V

DISCUSSION

5.1 Friction Values from Laboratory Testing

Several observations are made by examining the torque vs. rotation plots in Appendix B in conjunction with the behavior of the axial-torsional load frame during testing. Figure 5.1 compares both the initial torque vs. rotation (total) and the modified torque vs. plastic rotation. As seen in plots in Figure 5.1(a), the torque values are not constant which signifies a change in either the applied axial load or the radius of the contact area. During the tests, the specimen and pestle experience concentrated contact at high spots toward the edge of the specimen, which would cause a change in the axial force and torque values. To account for this eccentricity, the average work done by the friction forces is equated to the recorded energy in the hysteresis loop. The average applied axial load, P_T, is used in the energy balance formulation. Noticeable rotation of the axial-torsional load frame also occurred during testing, and can be seen in the sloping of the unloading curves in the torque vs. rotation plots at ±3 degrees or ±0.52 radians in Figure 5.1(b).

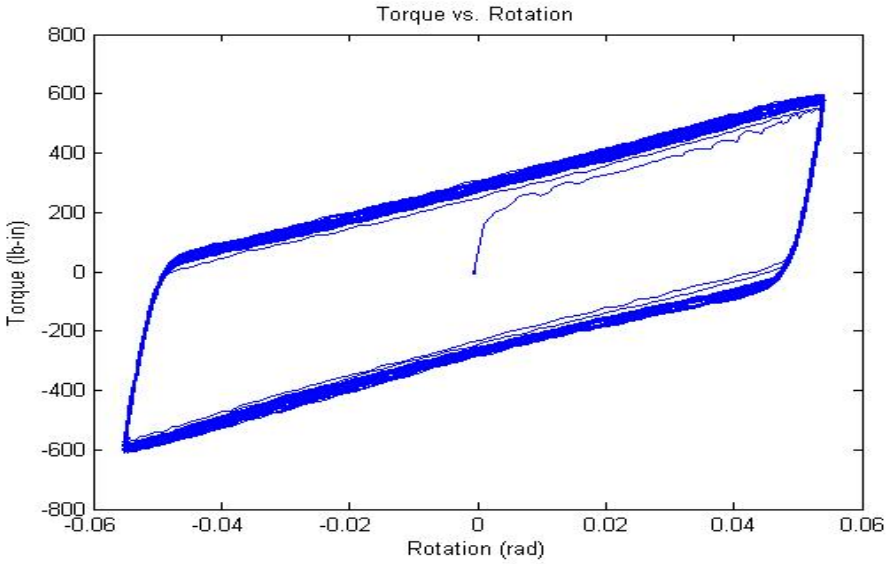

(a) Torque vs. Total Rotation

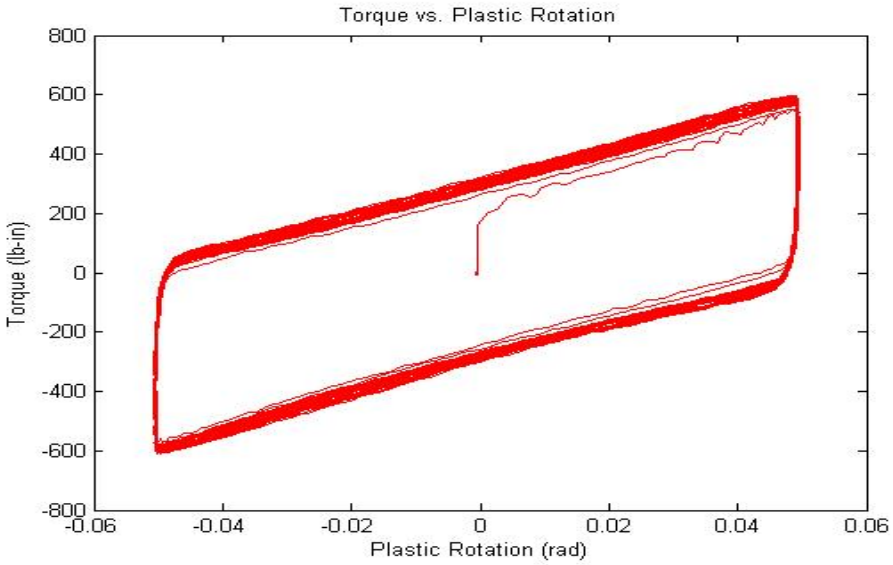

(a) Torque vs. Plastic Rotation

Figure 5.1: Comparison between Torque vs. Total Rotation
and Torque vs. Plastic Rotation

Ideally, the unloading curve of the torque vs. rotation would be perfectly vertical, but the rotation of the load frame introduced an additional elastic rotation. This was corrected by determining the slope, *m*, of the unloading line in the torque vs. total rotation plots and correcting the values by implementing the following formula

$$\phi_{zplastic} = \phi_z - \frac{T}{m}, \tag{5.1}$$

where T is the torque output and φ_z is the rotation specimen and is bounded by $\pm\theta_{zmax}$. This correction gives hysteresis loops that compensates for the energy in the unwanted elastic deformation of the load cell.

Friction coefficients for the tungsten carbide on steel and on itself fall into or just below the previously discussed desired range for minimum turning resistance without the adverse effects of hunting of 0.3. In practice with the introduction of siliceous fines and debris, it is unlikely that friction coefficient will remain as low as ideal laboratory conditions, so laboratory results slightly lower than the ideal range may be conducive to excellent performance. While the friction coefficients for extended service are unknown at this time, the tungsten carbide on tungsten carbide bearing interface gives values that are most conducive to low friction forces without excessive hunting as suggested by the literature (Simson and Pearce 2005, Tournay et al. 2006).

5.2 Wear Characteristics of Specimens

Both the materials of the coated specimens showed excellent wear characteristics throughout all tests. When compared to the damage incurred by the steel specimen, the polishing wear on the coated specimens is negligible.

As shown in Figures 4.3, 4.4, and 4.6, the wear patters on all specimens were local rather than uniform over the entire surface area. This localized contact is due to non uniform thicknesses of both the original steel specimens and the individual coatings.

Differences in thickness values of coated and uncoated specimens ranged from 0.001-0.01 inches. Before testing, tiny gaps between the specimen and the mortar were

documented in Figure 5.2. This gap suggests non-uniform contact and the presence of higher "hot spots." Slightly non-concentric rotation between the mortar and pestle resulted from hot spot contact.

Figure 5.2: Gap between Bearing Surfaces

Locally, the surface hotspots experienced a much higher stress state than the intended uniform stress caused by a 2 kip load on the full surface area. This unintended feature of the test gives evidence that the metallic protective coatings tested are quite robust, and while the proposed geometry will work to reduce stress concentrations, the protective coatings can withstand local stress increases. No cracking or spalling, even on the initially fractured coating of specimen #7, occurred throughout any test.

The black powdery substance found on the chrome nickel surfaces after testing is most likely free carbon. The plasma deposition process used to coat the specimens leaves the top of the coating less dense than the remaining coating and thus carbon can escape under the high pressure and torsion cause by the test. The specimens tested against the tungsten carbide pestle generally had more powder on the surfaces as seen in Figures 4.7 and 4.8.

Although no tests preformed were designed to test fatigue, some observations about the wear of the pestle can be made. The steel pestle experienced significant wear during each set of tests, and was sanded and polished to a 400 grit finish after each specimen was tested 3 times. The tungsten carbide pestle needed no such refinishing after each test, as only polishing of the surface occurred. No visible increase in wear occurred after the 21 tests performed using the coated pestle. Figure 5.3 shows the end condition of the tungsten carbide pestle resulting from repeated testing.

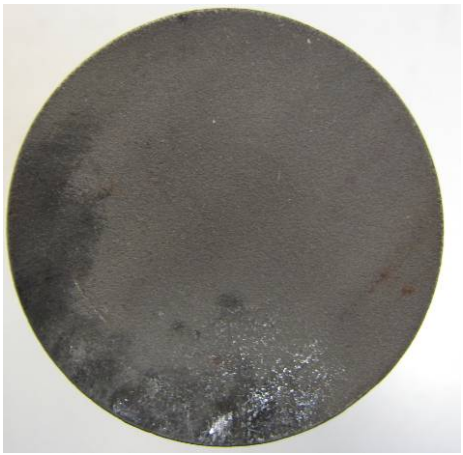

Figure 5.3: Tungsten Carbide Pestle After Testing

5.3 Full Scale Prototype

In general, railcar center plates are not precisely uniform; they vary from model to model and thus, an exact final geometry blanketing all possibilities is not practical. Instead, general design concepts are examined and should be implemented as variables. The appropriate radius of curvature must be greater than the height of the C.G. as measured from the center bowl face. With this satisfied, one can design inserts of desired thickness for a variety of truck geometry configurations. This can include an array of variances such as plate/bowl diameter, thickness, or implementation and specification of side bearings. Table 5.1 displays the car body rotation, lateral travel of

the center plate, and railcar height increase for varying values of insert radii of curvature and side bearing gaps for both 16 inch and 14 inch diameter center bowls. All assumptions concerning other truck geometry are listed in the MATLAB code in Appendix D.1.

Table 5.1: Kinematic Results from Various Initial Geometric Truck Parameters

		Side Bearing Gap of 1/16 in.			Side Bearing Gap of 1/4 in.		
	R_1 (in.)	θ_1 (deg.)	h (in.)	ΔH (in.)	θ_1 (deg.)	h (in.)	ΔH (in.)
Center Bowl Diameter of 14 in.	**128**	0.138	0.31	0.55	0.565	1.26	0.50
	90	0.138	0.22	0.63	0.56	0.88	0.58
	60	0.138	0.14	0.77	0.557	0.58	0.72
Center Bowl Diameter of 16 in.	**128**	0.138	0.31	0.61	0.565	1.26	0.55
	90	0.138	0.22	0.71	0.56	0.88	0.66
	60	0.138	0.14	0.88	0.557	0.58	0.84

Throughout the design of the inserts, a radius of curvature of 90 inches has been used as the basis for all geometric considerations. Table 5.1 shows that an increase in radius of curvature leads to less of an overall decrease in railcar height, but an increase in the overall horizontal travel of the center plate within the center bowl. From a retrofit point of view, the horizontal travel should be reduced first as less grinding modifications to existing truck components will be required. In manufacturing new center plates to incorporate this design, the entire center plate can be machined to include both the spherical cap of the insert and could have a thickness reduction to compensate for the change in height of the railcar. In this manufacturing scheme, no height increase would occur.

Concerns that are different for each instance of center bowl/center plate configurations are of equal importance. For instance, the method of attachment of the

center plate insert to the existing center plate should be established on an individual basis. The primary concern for the proper function of a spherical bearing interface is the ability of the railcar to rotate through the angle needed to close the gap at the side bearings. As mentioned in Chapter II and seen in Figure 2.4, the existing center plates, should be altered to accommodate the required rotation. With center plates and center plate inserts of differing diameter, a perimeter weld is one possible method of attachment. Figure 5.4 shows possible implementation of such an attachment scheme.

In future manufacturing of center plates, the actual face of the center plate could be machined as a convex piece and the overall thickness reduced to allow for the center bowl insert.

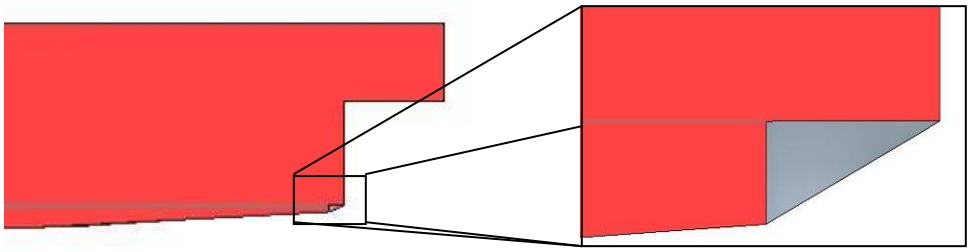

Figure 5.4: Center Plate Insert Connection and Weld Detail

The surface of hard contact side bearings could also be coated with tungsten carbide. Specifications for the type, size and, adjustment of side bearings vary tremendously, but the implementation of tungsten carbide as a coating during the manufacturing process would be a logical and immensely beneficial step. In addition to wear reduction, lower friction will reduce forces and greatly reduce the large moments caused by contact at the side bearings for both hard contact, and constant contact side bearings.

5.4 Dynamic Concerns for Design Inserts

The motion of the rotation of the railcar within the center bowl has been determined not to be oscillatory due to the enormous hysteretic damping of the frictional moment caused by center bowl forces. Because the maximum angle of rotation of the railcar is so small, the friction within the center bowl can be expected to significantly retard or completely stop the rotation of the railcar. With continuous random vibration from the motion of the train, the equilibrium caused by the large frictional moment will be intermittently broken and the railcar will work to right itself within the center bowl. This righting will be most prominent and beneficial in horizontal curves or other areas where vibration or rotation of the trucks. As a train enters a horizontal curve, inertial forces act on the C.G. of the railcar and cause it to rotate counter clockwise about the I.C. The weight of the railcar will cause clockwise rotation about the I.C. back towards its stable position.

The purpose of the dynamic analysis presented in this project is to confirm that the rotation of the railcar within the center bowl will not be detrimental to the function of the railcar. It is necessary for more involved dynamic models of the system to be studied to ascertain any other areas of concern. Such analysis could include the exploration of multiple DOF models or more advanced models for the contact stress within the center bowl. The assumption of uniform pressure is an approximation, as the exact contact stress is unknown. Using a uniform contact pressure gives excellent closed form approximations to the moment of the friction force about the I.C. As mentioned in Appendix A.1, values of interest such as friction moment have been determined both exactly and under the assumption that the spherical cap over which the contact pressure acts can be well approximated by a circular area.

For static equilibrium of the railcar to exist, the resultant of the force from the contact pressure and frictional force must be vertical and pass through the centroid of the railcar. In the static problem, a uniform contact pressure does not allow for equilibrium, as the resultant force would pass through the I.C. at a location not directly vertically under the centroid. As shown in Appendix A.1, this error is likely negligible.

5.5 Constant Contact Side Bearings

Constant contact side bearings are becoming increasingly popular for heavy railcars. Unlike hard-faced side bearings with specific gaps as discussed above, constant contact side bearings are often preloaded spring systems. Clearly the introduction of springs in place of a gap at the side bearings changes the kinematic formulations for rotation of the railcar body in Chapter II. Optimizing side bearing stiffness is a worthy endeavor as high stiffness causes higher forces and thus higher turning moments, and must be balanced with larger car body rotations caused by low stiffness.

The presence of springs at the side bearings will also alter the EOM presented in Chapter II. Springs will alter the natural frequency and thus the damping ratio.

5.6 Future Testing

This thesis outlines the geometric components of the proposed center bowl/ center plate inserts and shows, through preliminary laboratory testing, a robust implementation of protective coating material properties to improve the bearing interface interaction. Other needed research includes material research examining the deposition of ceramic materials such as silicon nitride or silicon carbide onto steel. Tests on concave or convex specimen surfaces would also improve the understanding of the performance of protective coating on the system.

In addition to center bowl/center plate interface modifications, other application of a protective wear would be beneficial. A vertical wear liner coated with tungsten carbide would mitigate wear from the necessary contact between the center plate and center bowl walls.

As the environment of the center bowl bearing interface is immensely complicated, full scale testing of insert prototypes could be used to confirm the results of this work and determine areas of improvement for the design.

CHAPTER VI

CONCLUSIONS

Based on geometric designs and laboratory testing, the following conclusions regarding the proposed center bowl/center plate inserts have been made.

- An I.C. higher than the C.G. of the railcar ensures stability of the railcar upon the proposed center bowl/center plate interface under standard use.

- Slight modification of existing components is required to achieve flush contact at the spherical bearing interface through the use of 2 spherical bearing inserts.

- With the trend of reduction of the distance *g* to 1/16 inch, the kinematics of the rotation of the railcar body within the center bowl is accommodated by an *h* of 0.22 inches. The proposed geometric inserts increase the total height of the railcar by 0.71 inches.

- Dynamic amplification of the rotation within the center bowl is impossible due to the damping ratio of 240 caused by friction.

- The proposed spherical bearing surface will work to distribute stresses more evenly by creating more uniform contact area and re-centering the rotation of the center plate away from the center bowl rim. The center bowl rim will still provide necessary lateral force resistance.

- Tungsten carbide coated test specimens give friction coefficients consistent with the optimum friction coefficient for this application of 0.3 (Simson and Pearce 2005).

- While the steel specimen experienced substantial pitting and permanent local surface deformations, the tungsten carbide coated surfaces were polished with no perceptible change in thickness.

- The proposed design is a practical and robust implementation of tungsten carbide coating to reduce both center bowl/center plate bearing surface wear and turning moments caused by a high friction coefficient between the bearing surfaces.

- Coating of hard contact and constant contact side bearings with tungsten carbide will improve wear at the side bearing surface, but will also reduce contact forces that contribute largely to turning moments.

REFERENCES

Association of American Railroads (1981). *Manual of Standards and Recommended Practice*, Association of American Railroads, Washington, D.C.

Callister, Jr. , W. D. (2003). *Fundamentals of Materials Science and Engineering*, John Wiley & Sons, Inc., New York.

Chopra, A.K. (2001). *Dynamics of Structures*, Prentice Hall, Upper Saddle River, New Jersey.

Hay, W. W. (1982). *Railroad Engineering*, John Wiley & Sons, New York.

Lide, D. R., ed. (2005). *CRC Handbook of Chemistry and Physics*, 86th ed., Taylor and Francis, New York.

Simson, S.A., and Pearce, M. (2005). "Longitudinal Impact Forces at 3 Piece Bogie Center Bearings." *Proc., Joint Rail Conference*, Association of American Railroads (AAR), Pueblo, CO.

Stewart, J. (1999). *Calculus: Early Vectors*, Brooks/Cole Publishing Co., New York.

Tournay, H.M., Lang, R., and Wolgram, T. (2006). "Performance History and Teardown Results of a Coal Car Identified as a Poor Performer While Passing Loaded Across a Truck Performance Detector." *Transportation Technology Center, Report No. R-976*, American Association of Railroads, Pueblo CO.

Wolf, G. (2005a). "The Truck Bolster Bowl: Is It a Bowl or a Bearing?" *Interface-The Journal of Wheel/Rail Interaction*, < http://www.interfacejournal.com/> (Feb. 16, 2006).

Wolf, G. (2005b). "Vehicle Side Bearings: Function, Performance and Maintenance" *Interface-The Journal of Wheel/Rail Interaction*, <http://www.interfacejournal.com/> (May 3, 2007).

Wolf, P.R., and Ghilani, C.D. (2006). *Elementary Surveying*, Pearson Prentice Hall, Upper Saddle River, New Jersey.

APPENDIX A

DERIVATIONS

A.1 Derivation of Moment Due to Friction

In order to determine the moment resulting from the friction traction on the surface of center plate insert, spherical coordinates can be employed. The infinitesimal surface area, *dS* is

$$dS = R_1^{\,2} \sin\varphi_s \, d\varphi_s \, d\theta_s \,. \tag{A.1}$$

where:

$0 < \theta_s < 360$ degrees

$0 < \varphi_s < \varphi = 4.95$ degrees (See Equation 2.15)

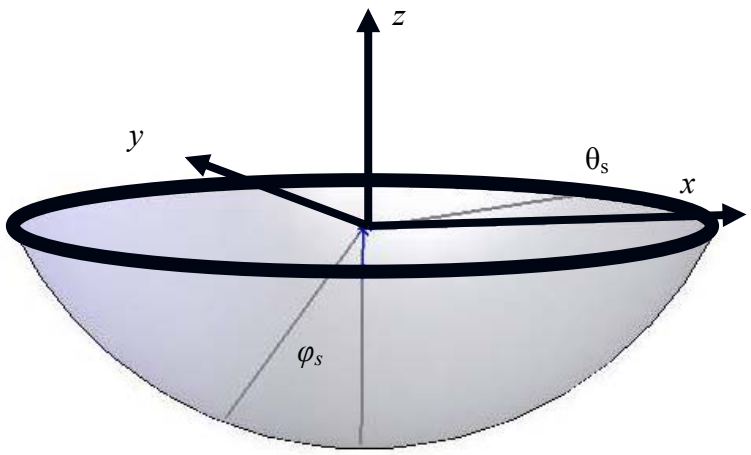

Figure A.1: Spherical Coordinate Angles on a Spherical Cap

The vertical component of the resultant force from a uniform pressure (p) is

$$N_v = \int p\cos(\varphi_s) dS \tag{A.2}$$

$$N_v = \int_0^{\varphi} \int_0^{2\pi} p\cos(\varphi_s) R_1^2 \sin(\varphi_s) d\theta \; d\varphi_s = \pi p R_1^2 \int_0^{\varphi} \sin(2\varphi_s) d\varphi_s \tag{A.3}$$

$$N_v = \pi p R_1^2 \frac{1-\cos(2\varphi)}{2}. \tag{A.4}$$

Substituting in W for N_v the pressure is

$$p = \frac{2W}{\pi R_1^2 \left(1-\cos(2\varphi)\right)}. \tag{A.5}$$

The friction traction is

$$\sigma_T = \frac{2W\mu}{\pi R_1^2 \left(1-\cos(2\varphi)\right)}. \tag{A.6}$$

The moment caused by this traction varies over the surface of the spherical cap. The moment arm from the I.C. to an arbitrary infinitesimal surface area, dS is

$$L = \sqrt{y^2 + z^2}, \tag{A.7}$$

or in spherical coordinates

$$L = \sqrt{\left(R1\sin^2\varphi_s \sin\theta_s\right)^2 + \left(R1\cos\varphi_s\right)^2}. \tag{A.8}$$

The moment from friction is

$$M_f = \int \mu p L dS \tag{A.9}$$

$$M_f = \mu p R_1^2 \int_0^{\varphi}\int_0^{2\pi} \sqrt{\left(R1\sin\varphi_s \sin\theta_s\right)^2 + \left(R1\cos\varphi_s\right)^2}\, \sin(\varphi_s) d\theta_s d\varphi \quad . \tag{A.10}$$

The MATLAB code in Appendix D.2 was used in the numerical integration of M_f, and the numerical value of M_f is 7729200 inch-pounds.

Due to the small angle φ, the surface area of the spherical cap is very close to the surface area of a flat circular region. If taken to be a flat circular area the following values for pressure is obtained

$$p \approx \frac{W}{\pi \frac{d_c^{\,2}}{4}}. \tag{A.11}$$

The moment resulting from this pressure distribution is

$$M_f \approx \mu R_1 W. \tag{A.12}$$

A comparison of the numerical values of the exact expressions and the approximate expressions are shown in the table below.

Table A.1: Comparison of Exact and Approximate Values for Pressure and Moment

	Exact Value	Approximate Value	% Error
p (psi)	1503.5	1515.7	0.80
M_f(lb-in)	7729200	7722000	-0.09

As the resulting values have such low percent error, the approximate expressions have been used in developing expression for damping ration in Chapter II.

A.2 Derivation of Relationships between Work Done by Friction and Hysteretic Energy

A relationship between the following parameters was developed to obtain the friction coefficient from data gathered during testing: Axial Force (P_T), torque (T), friction coefficient (μ), and angle of rotation (θz).

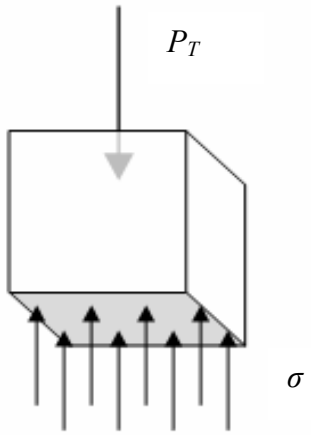

Figure A.2: Free Body Diagram of a Body in Compression

The pressure distribution shown in Figure A.2 was assumed to be uniform over the area (A)

$$\sigma = \frac{P_T}{A}. \tag{A.13}$$

Shear stress from coulomb friction is defined as

$$\tau = \mu\sigma, \tag{A.14}$$

or combining (A.13) and (A.14), the shear stress is

$$\tau = \mu\sigma = \mu\frac{P_T}{A}. \tag{A.15}$$

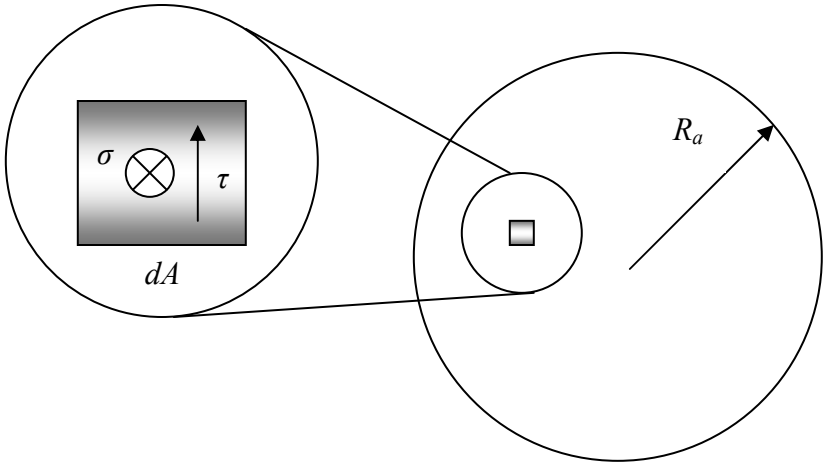

Figure A.3: Infinitesimal Area on Circular Cross- Section

Assuming this contact surface is subject to both a compressive normal force (P_T) and a frictional counter-clockwise torsion (*T*), an infinitesimal surface area (*dA*) will experience an infinitesimal normal force (*dN*) and an infinitesimal in-plane force (*dH*) from friction.

The horizontal force on the area, *dA*, was defined using (A.15) from above

$$dH = \tau\, dA = \mu \frac{P_T}{\pi R_a^{\,2}} dA . \tag{A.16}$$

The infinitesimal torque, *dT*, is defined as (See Figure A.4)

$$dT = rdH = r\,\mu \frac{P_T}{\pi R_a^{\,2}} dA . \tag{A.17}$$

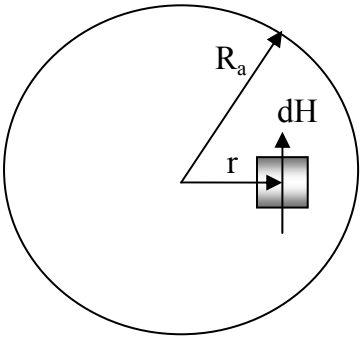

Figure A.4: Components Infinitesimal Torque

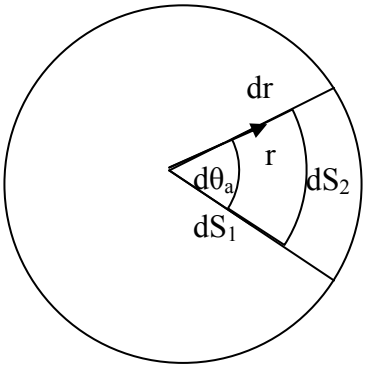

Figure A.5: Illustration of the Polar Rectangle

Torque over the entire surface is found by integrating over the surface using polar coordinates. The following equations were developed to find the infinitesimal area (*dA*) for a polar rectangle

$$S = r\,\theta \tag{A.18}$$

$$dS_1 = (r - \frac{dr}{2})\, d\theta_a \tag{A.19}$$

$$dS_2 = (r + \frac{dr}{2})\, d\theta_a \tag{A.20}$$

$$dA = \frac{dr}{2}\left[\left(r - \frac{dr}{2}\right)d\theta_a + \left(r + \frac{dr}{2}\right)d\theta_a\right] \tag{A.21}$$

$$dA = r\, dr\, d\theta_a . \tag{A.22}$$

Combining (A.17) and (A.22), infinitesimal torque, *dT*, becomes

$$dT = r\,\mu \frac{P_T}{\pi R_a^{\,2}} r\, dr\, d\theta_a . \tag{A.23}$$

The work energy of this torque if found by multiplying dT by the rotation as follows

$$dW_E = r\,\mu \frac{P_T}{\pi R_a^{\,2}} r\, dr\, d\theta_a d\phi_z . \tag{A.24}$$

Integrating over the surface area, the total work is

$$W_E = \frac{\mu P_T}{\pi R_a^{\,2}} \int_0^{2\pi} \int_0^{R_a} \int_{-\theta_{z\max}}^{\theta_{z\max}} r^2 dr d\theta_a d\phi_z \tag{A.25}$$

$$W_E = \frac{4}{3}\mu P_T R_a \theta_{z\max} , \tag{A.26}$$

and rearranging, the friction coefficient is

$$\mu = \frac{3W_E}{4P_T R_a \theta_{z\max}}. \tag{A.27}$$

Equating the work done by this force to the energy in the hysteresis loop

$$\mu = \frac{3E_L}{4P_T R_a \theta_{z\max}}. \tag{A.28}$$

APPENDIX B

TEST DATA PLOTS

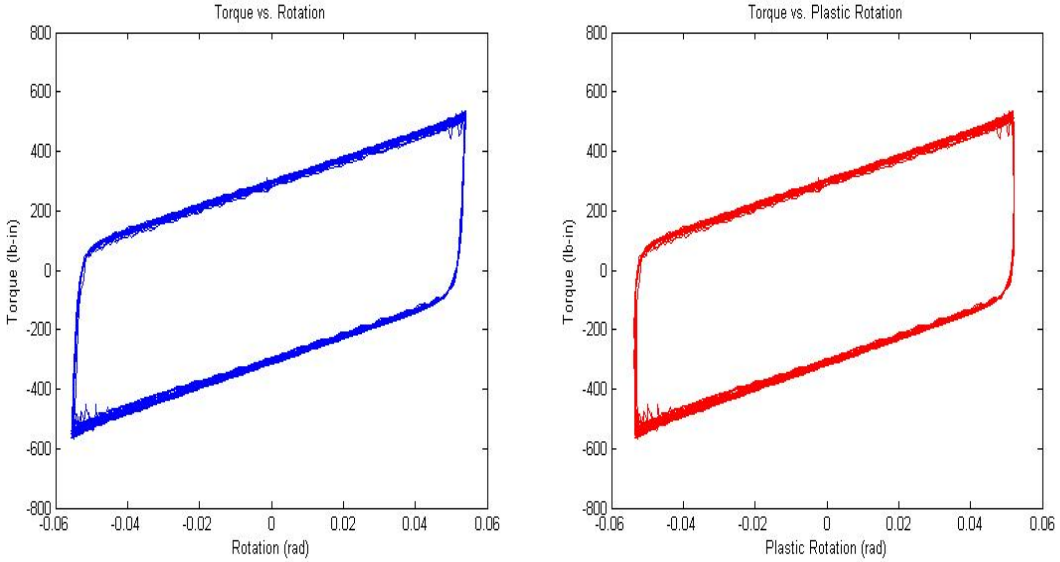

Figure B.1: Test Data Plots for Specimen 1 (Tungsten Carbide) on Steel

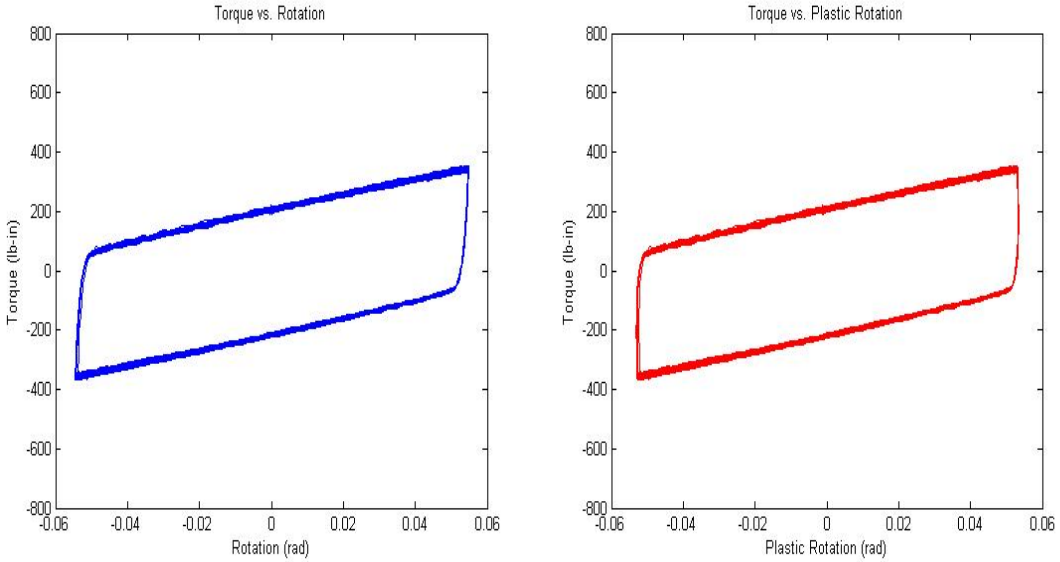

Figure B.2: Test Data Plots for Specimen 2 (Tungsten Carbide) on Steel

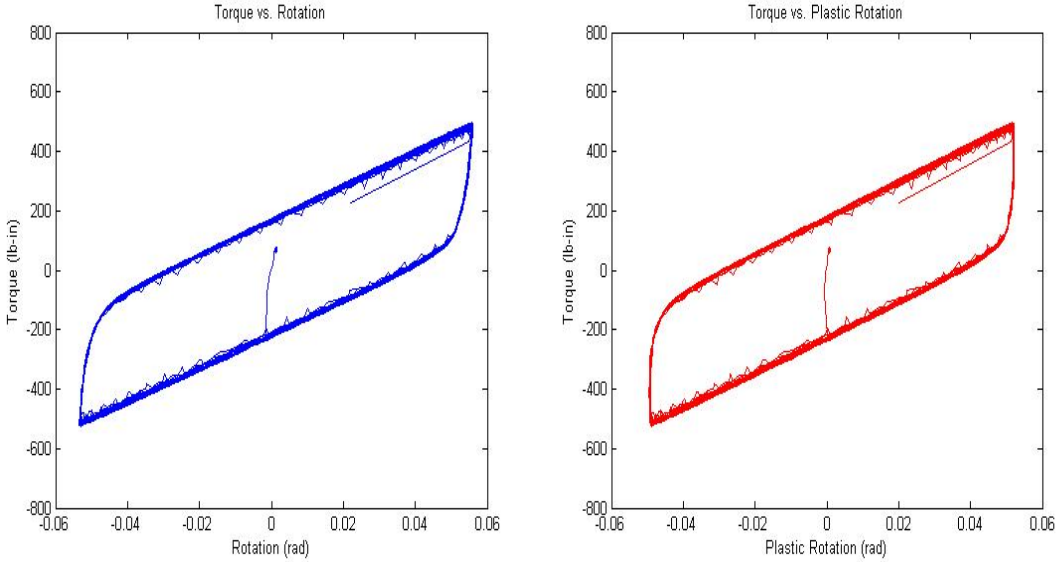

Figure B.3: Test Data Plots for Specimen 3 (Tungsten Carbide) on Steel

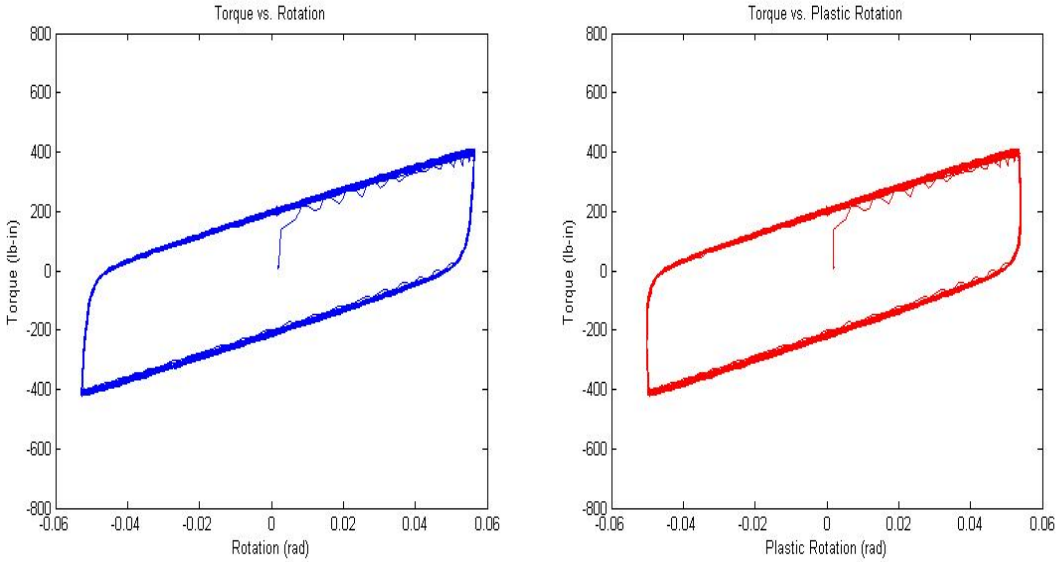

Figure B.4: Test Data Plots for Specimen 4 (Tungsten Carbide) on Steel

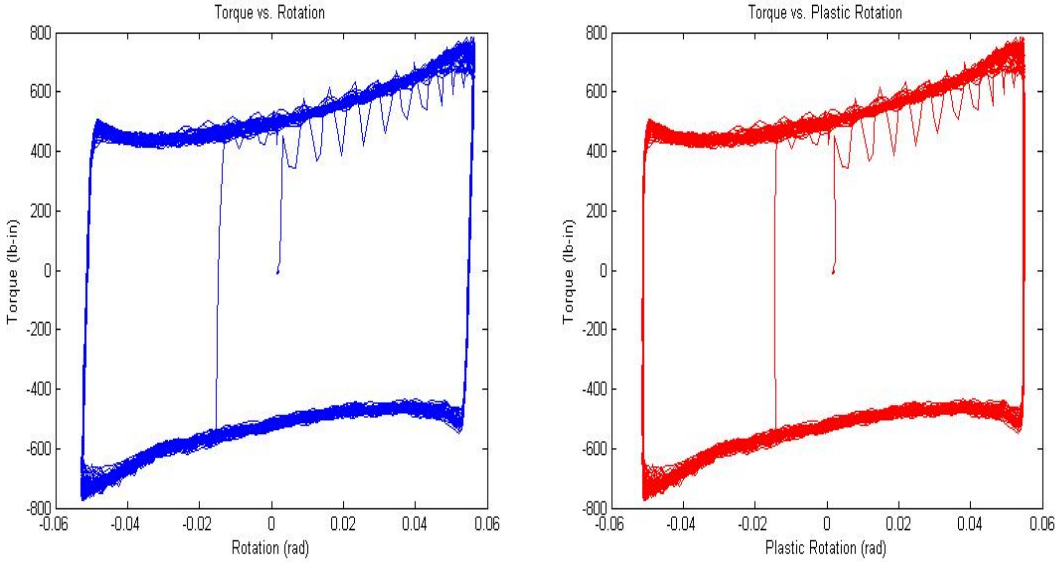

Figure B.5: Test Data Plots for Specimen 5 (Chrome Nickel) on Steel

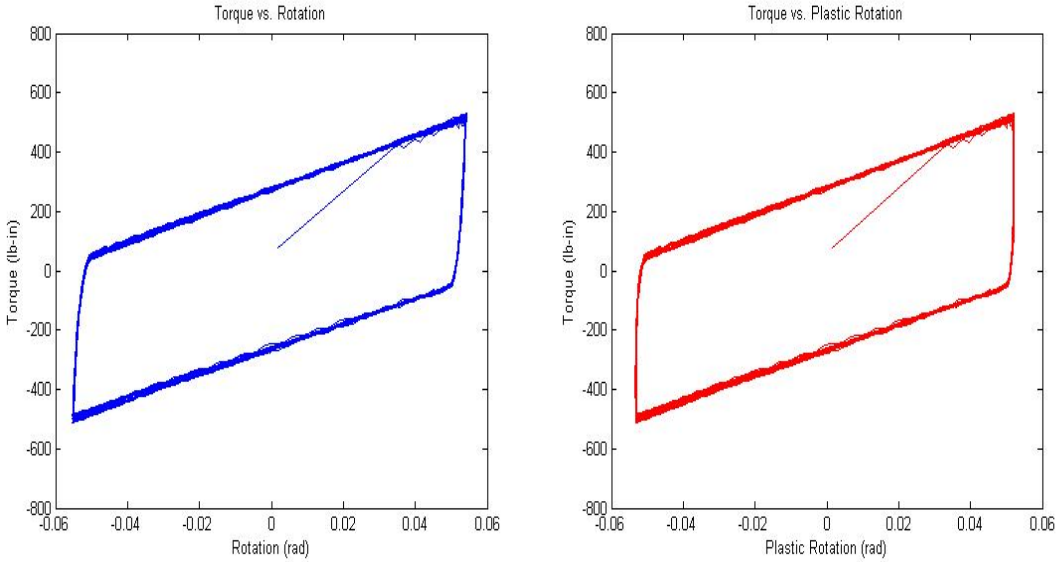

Figure B.6: Test Data Plots for Specimen 6 (Chrome Nickel) on Steel

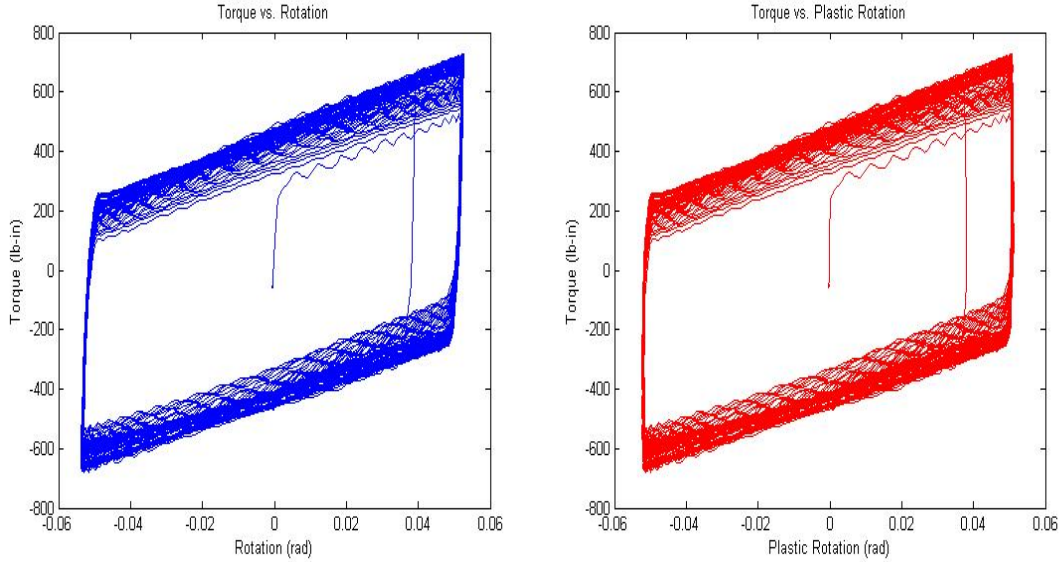

Figure B.7: Test Data Plots for Specimen 7 (Chrome Nickel) on Steel

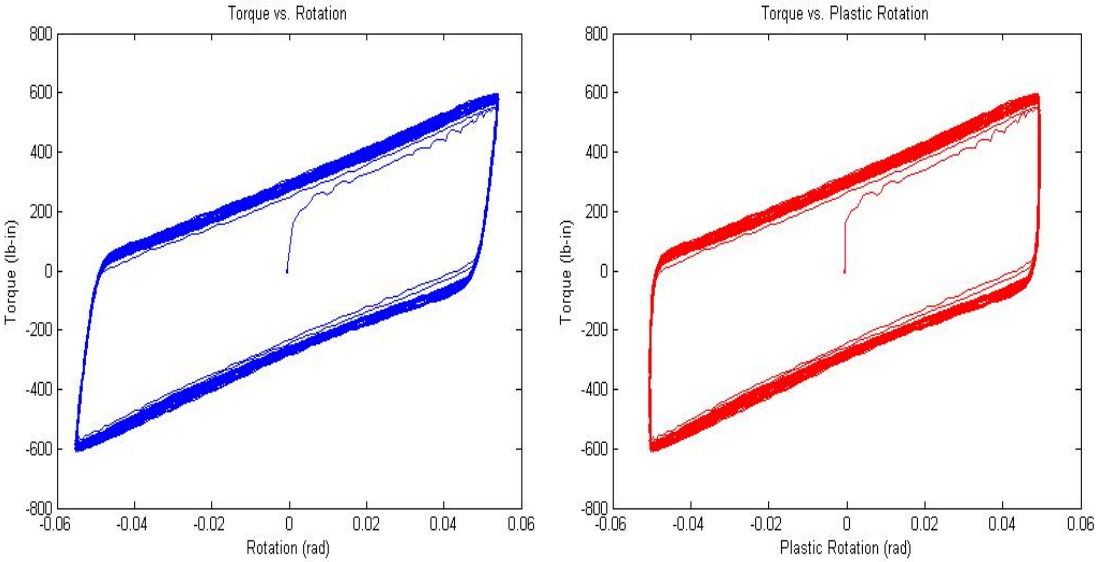

Figure B.8: Test Data Plots for Specimen 12 (Steel) on Steel

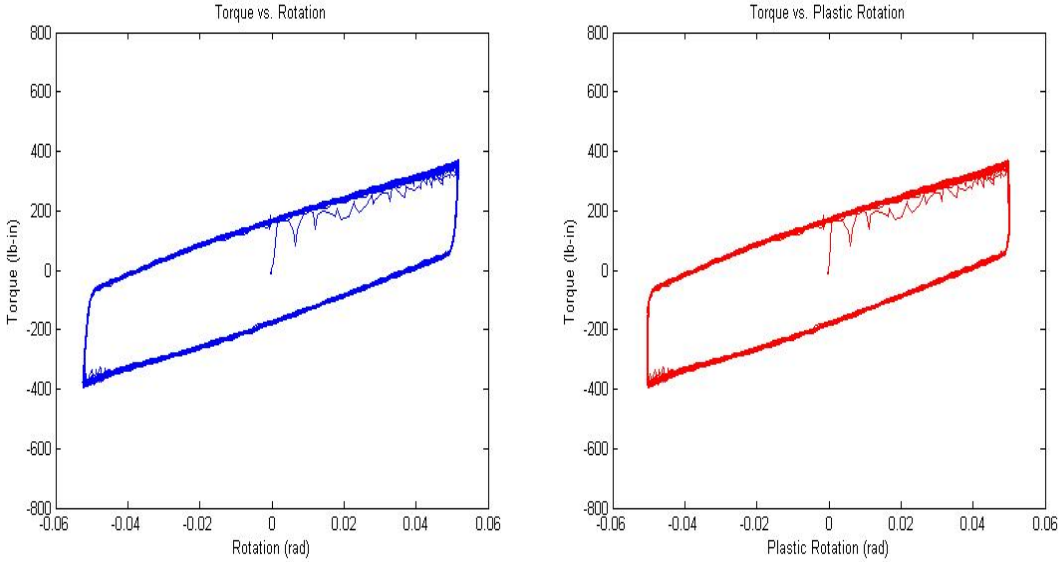

Figure B.9: Test Data Plots for Specimen 1 (Tungsten Carbide) on Tungsten Carbide

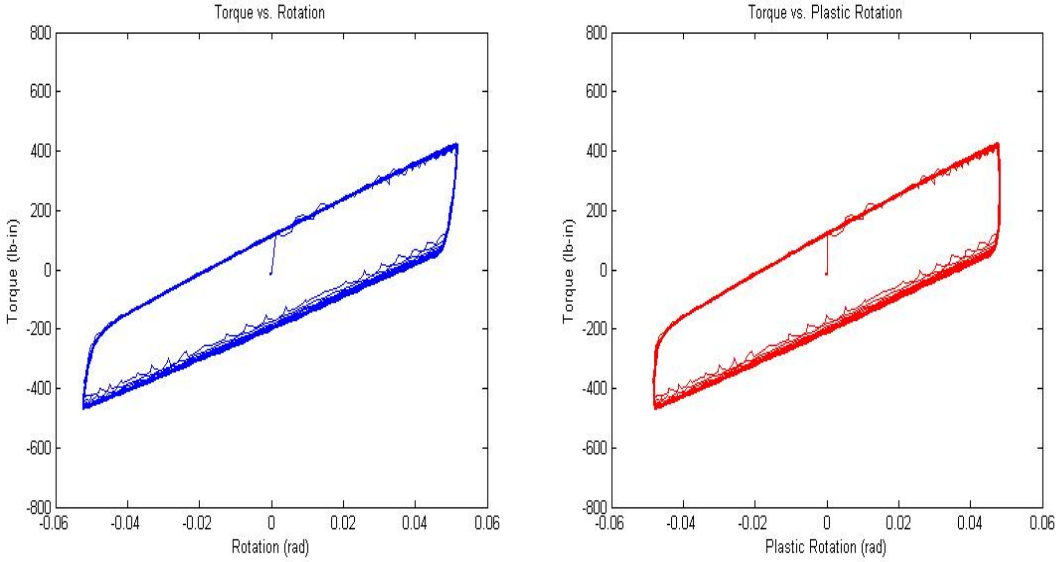

Figure B.10: Test Data Plots for Specimen 2 (Tungsten Carbide) on Tungsten Carbide

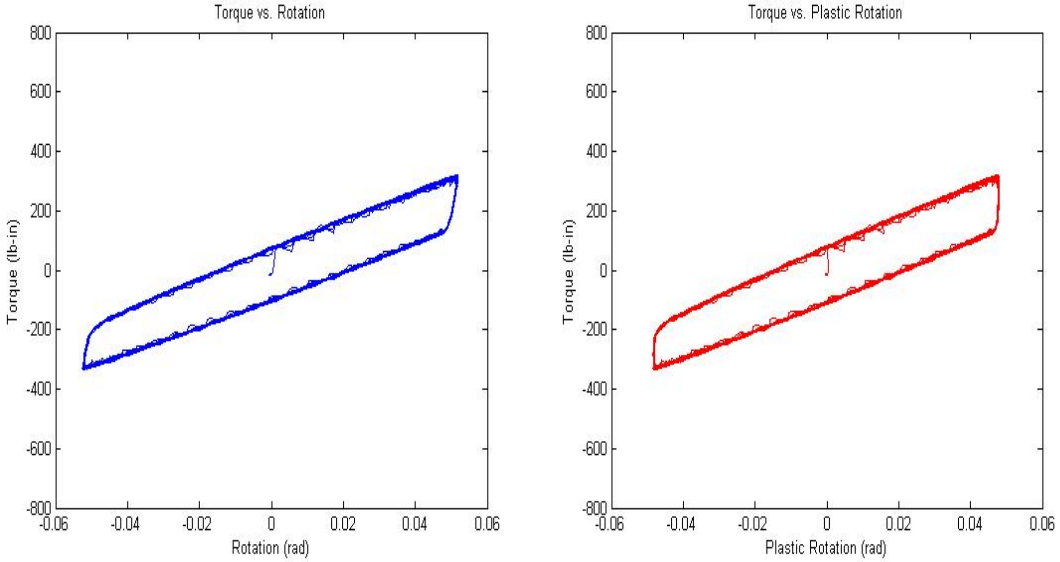

Figure B.11: Test Data Plots for Specimen 4 (Tungsten Carbide) on Tungsten Carbide

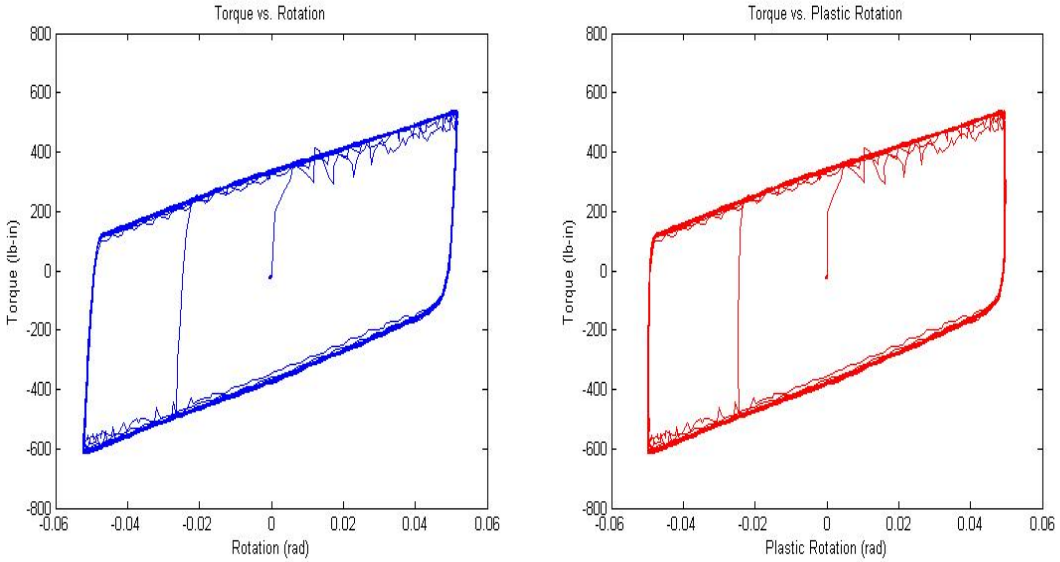

Figure B.12: Test Data Plots for Specimen 5 (Chrome Nickel) on Tungsten Carbide

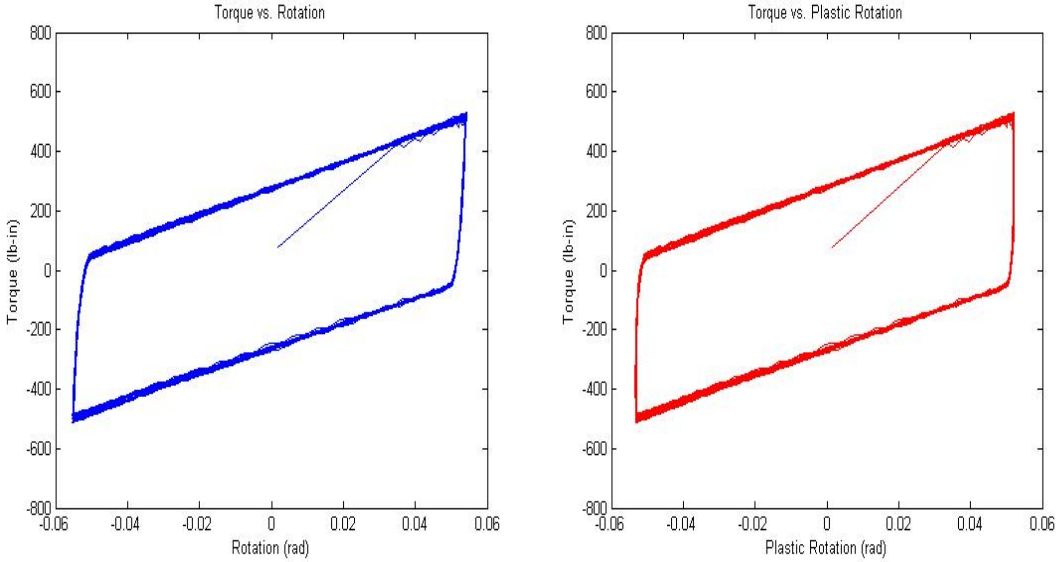

Figure B.13: Test Data Plots for Specimen 6 (Chrome Nickel) on Tungsten Carbide

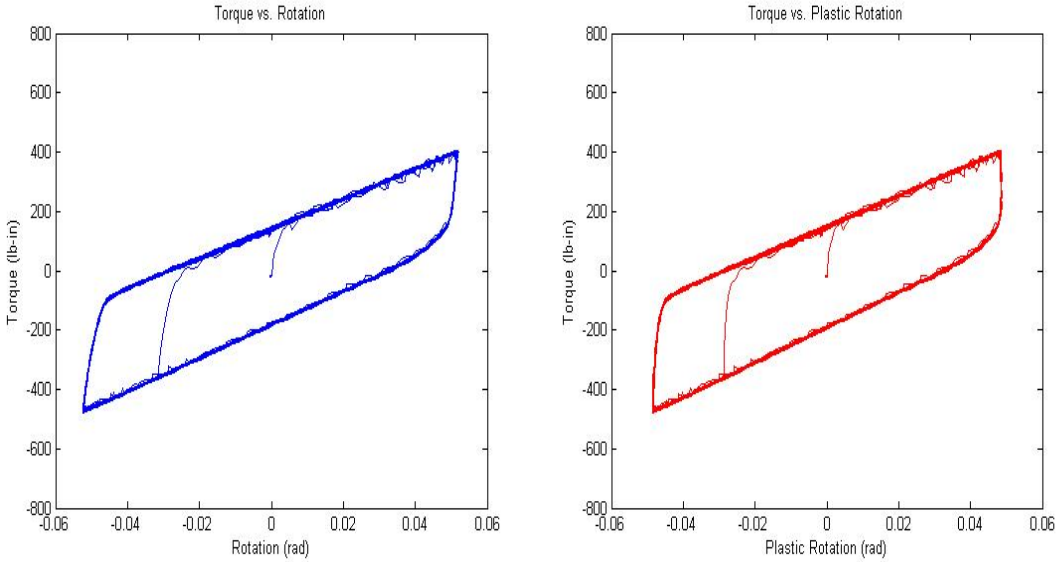

Figure B.14: Test Data Plots for Specimen 7 (Chrome Nickel) on Tungsten Carbide

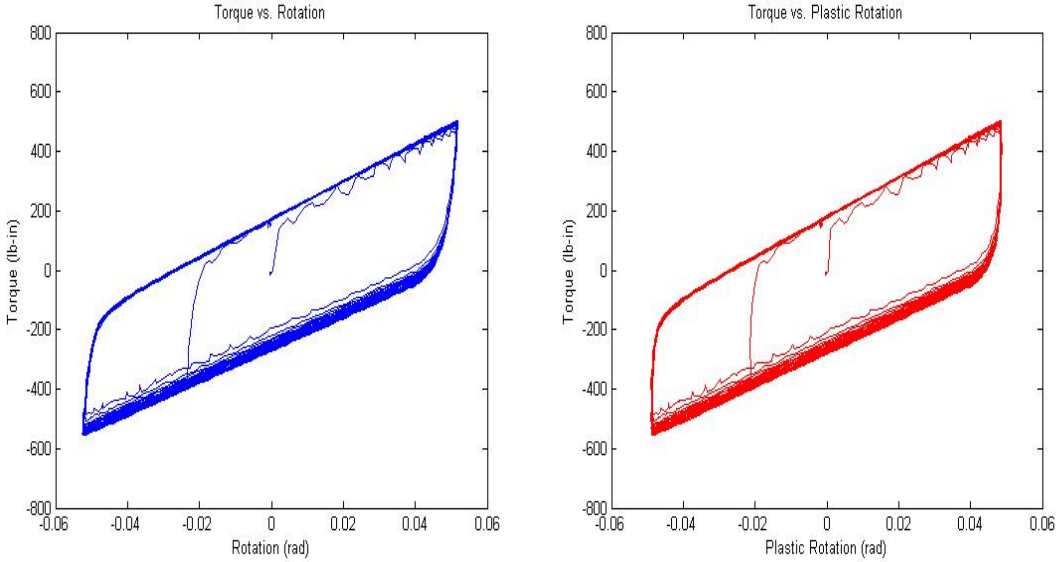

Figure B.15: Test Data Plots for Specimen 12 (Steel) on Tungsten Carbide

APPENDIX C

SPECIMEN PHOTOGRAPHS

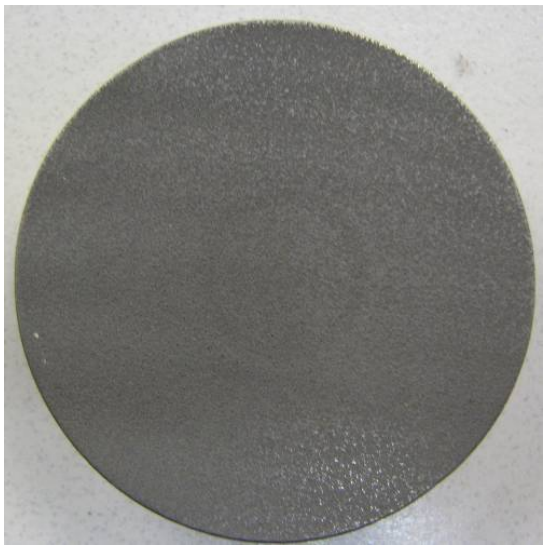

(a) Before Testing

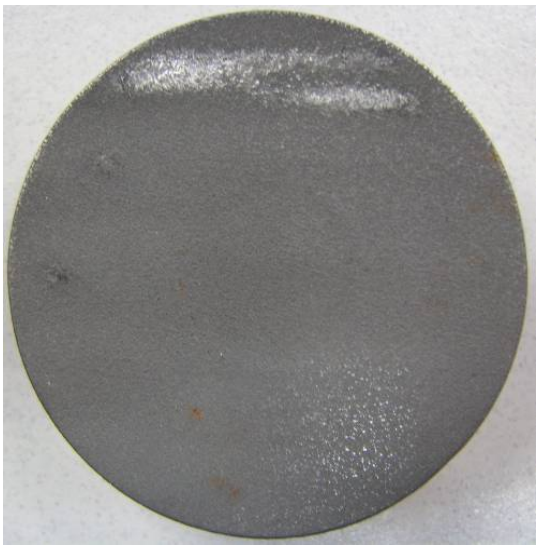

(b) After Steel Pestle Testing

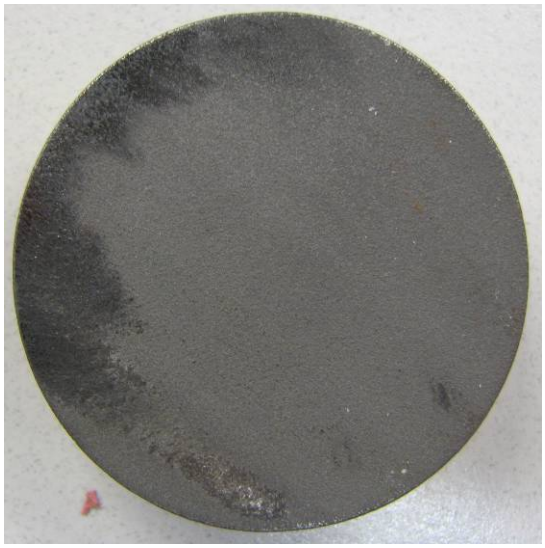

(c) After Tungsten Carbide Pestle Testing

Figure C.1: Specimen #1 Before and After Testing

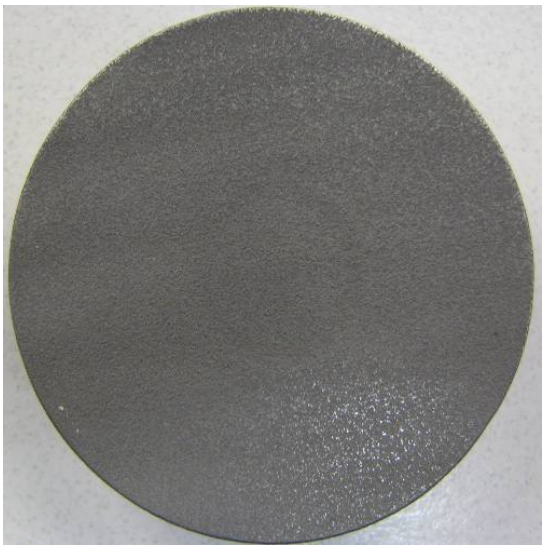

(a) Before Testing

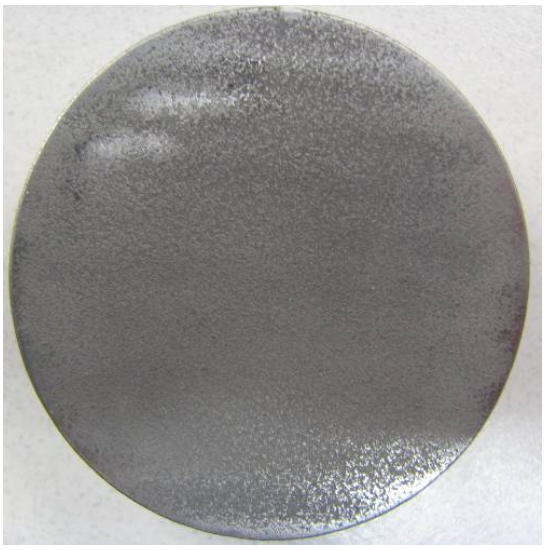

(b) After Steel Pestle Testing

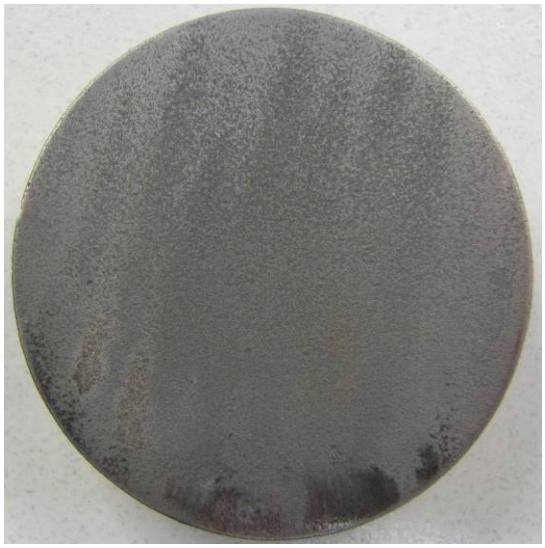

(c) After Tungsten Carbide Pestle Testing

Figure C.2: Specimen #2 Before and After Testing

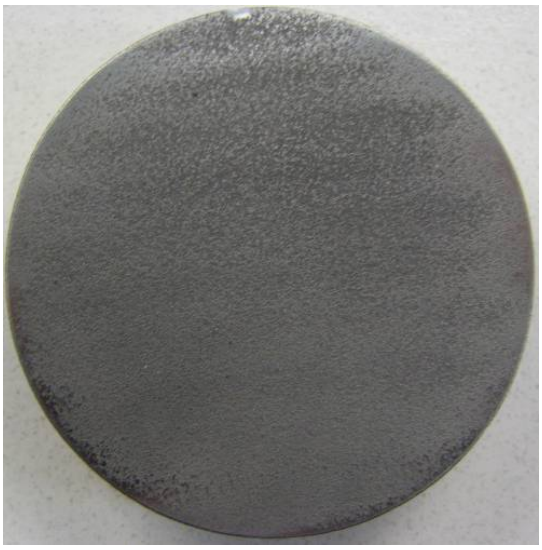

(a) Before Testing

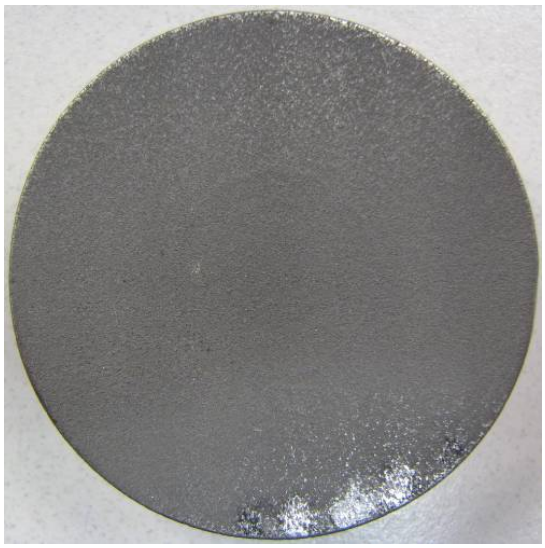

(b) After Steel Pestle Testing

Figure C.3: Specimen #3 Before and After Testing

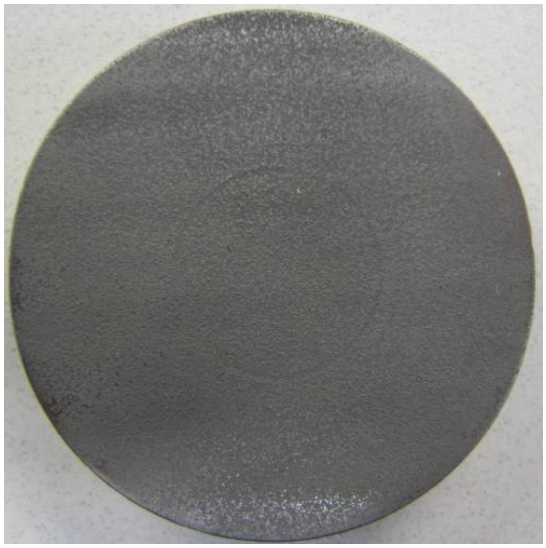

(a) Before Testing

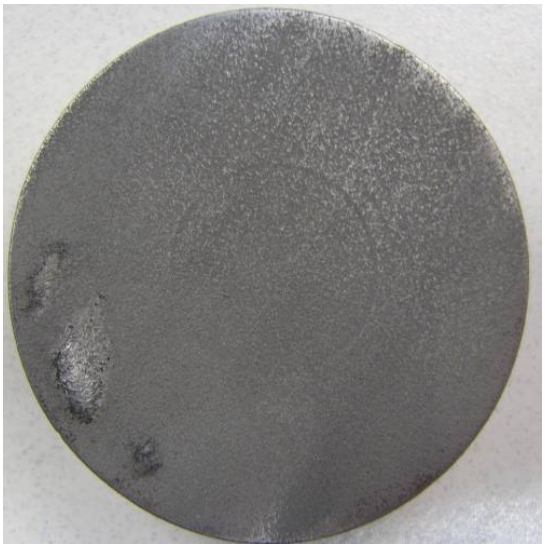

(b) After Steel Pestle Testing

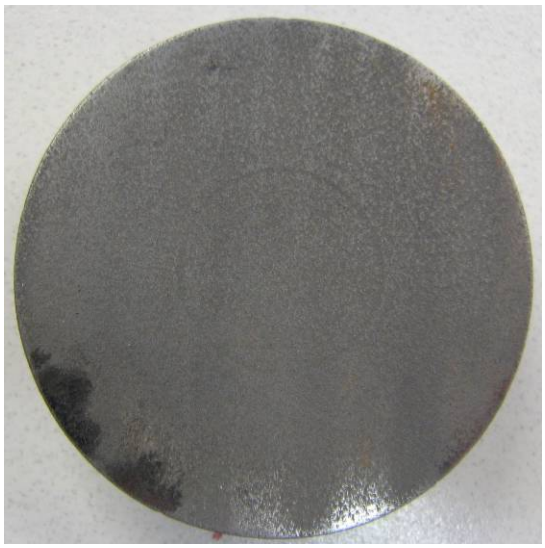

(c) After Tungsten Carbide Pestle Testing

Figure C.4: Specimen #4 Before and After Testing

(a) Before Testing

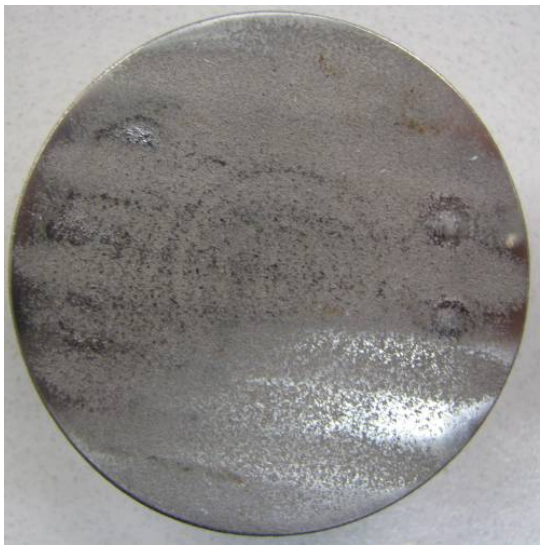

(b) After Steel Pestle Testing

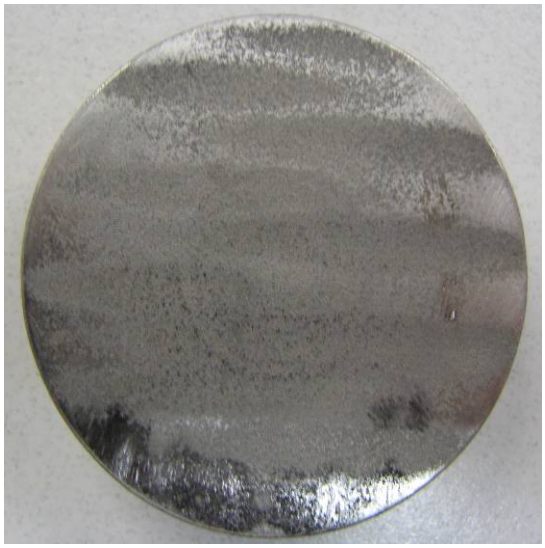

(c) After Tungsten Carbide Pestle Testing

Figure C.5: Specimen #5 Before and After Testing

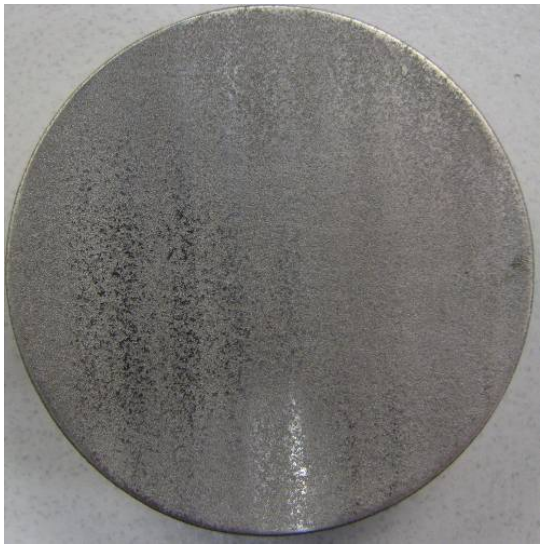

(a) Before Testing

(b) After Steel Pestle Testing

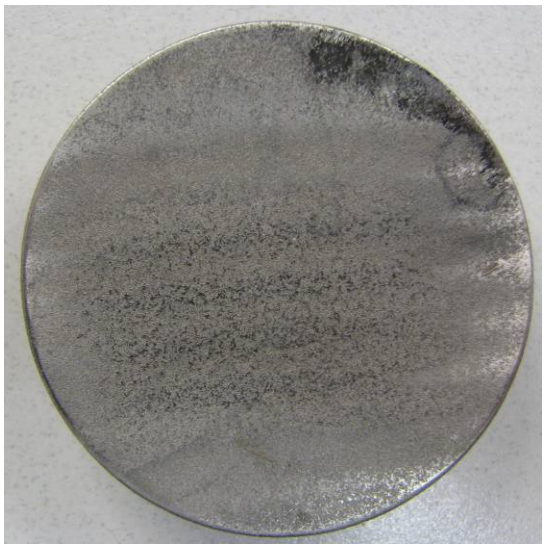

(c) After Tungsten Carbide Pestle Testing

Figure C.6: Specimen #6 Before and After Testing

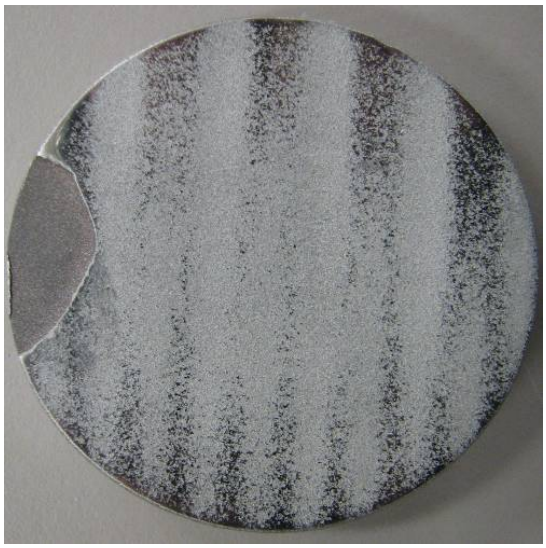

(a) Before Testing

(b) After Steel Pestle Testing

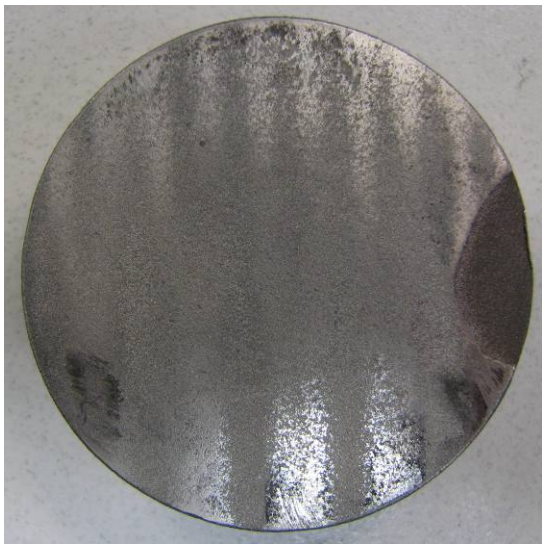

(c) After Tungsten Carbide Pestle Testing

Figure C.7: Specimen #7 Before and After Testing

(a) Before Testing

(b) After Steel Pestle Testing

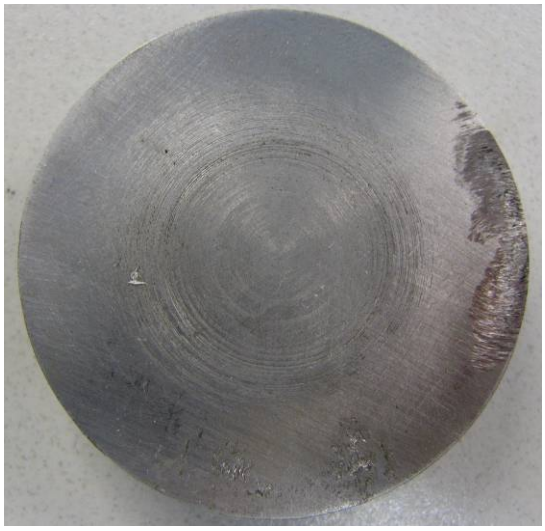

(c) After Tungsten Carbide Pestle Testing

Figure C.8: Specimen #12 Before and After Testing

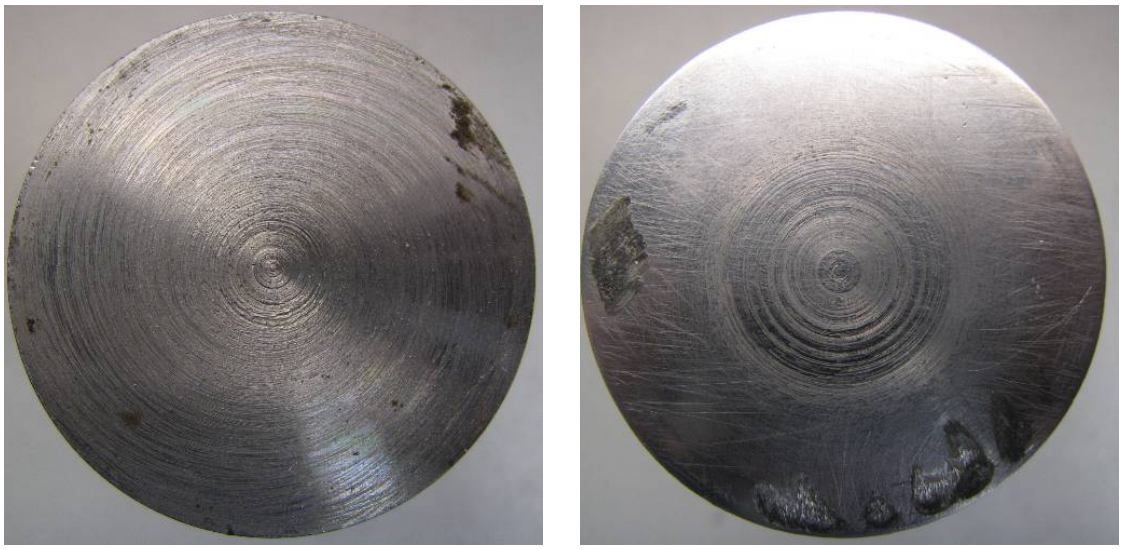

(a) Before Testing (b) After Testing

Figure C.9: Steel Pestle Before and After Steel Pestle Testing

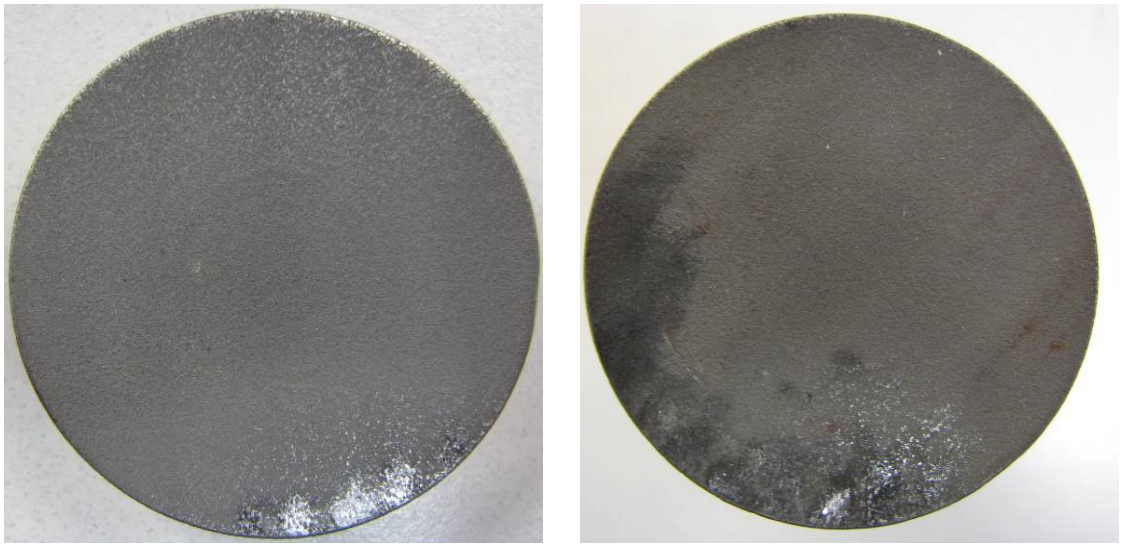

(a) Before Testing (b) After Testing

Figure C.10: Tungsten Carbide Pestle Before and After Tungsten Carbide Pestle Testing

APPENDIX D

MATLAB CODE

D.1 MATLAB Code for Kinematic Relationships

```
%%MATLAB Code for Kinematic Relationships and Geometric Design
%%Calculations for Inserts



clear
clc

%%Input
CG=60;          %Center of Gravity of Railcar above Center Bowl
                %Face (in.)
R1=1.5*CG;      %Radius of Curvature of Bearing Interface (in.)
ti=0.25;        %Inner(Middle)Thickness of Bottom Insert (in.)
d=16;           %Diameter of Center Bowl

%%Calculation of Outer Thickness of Bottom Insert
to=R1-sqrt(4*R1^2-d^2)/2+ti;    %Outer Thickness of Bottom Insert (in.)

%%Exploration of Kinematic Relationships

g=1/16;         %Side Bearing Gap (in.)
b1=4.5;         %Truck Side Bearing Height from Bolster Surface (in.)
b2=b1+g;        %Car Body Side Bearing Height from Bolster
                %Surface (in.)
a=26;           %Horizontal Distance between Side Bearings and
                %Center Bowl Center (in.)

%%Calculations of Needed Quantities from Defined Geometry

%%Vertical Side Bearing Gap and Subsequent Rotation

R2=sqrt(a^2+(R1+ti-(b2))^2);        %Radius from I.C. to Car Body
                                    %Side Bearings (in.)
gamma =atan(a/((R1+ti-(b2))));      %Angle between Car Body Side
                                    %Bearings and Vertical (rad.)
gammad=gamma*180/pi;                %Angle between Car Body Side
                                    %Bearings and Vertical (deg.)
alpha=acos(g/R2+cos(gamma));        %Difference Between Gamma and
                                    %Theta (rad.)
alphad=alpha*180/pi;                %Difference Between Gamma and
                                    %Theta (deg.)

theta1=gamma-alpha;                 %Rotation Required to Close Side
                                    %Bearing Gap (rad.)
theta1d=theta1*180/pi;              %Rotation Required to Close Side
                                    %Bearing Gap (deg.)

%%Horizontal Side Bearing Movement Due to Rotation

gh=a-R2*sin(alpha);                 %Horizontal Movement of Side
```

```
                                    %Bearings (in.)

%%Horizontal Center Bowl Gap and Subsequent Rotation

beta=asin((d/2)/R1);                %Angle Between Center Bowl Rim
                                    %and Horizontal (rad.)
betad=beta*180/pi;                  %Angle Between Center Bowl Rim
                                    %and Horizontal (deg.)
phi=beta-theta1;                    %Angle Between Beta and
                                    %Theta1* (rad.)
phid=phi*180/pi;                    %Angle Between Beta and
                                    %Theta1* (deg.)

h=R1*sin(beta)-R1*sin(phi);         %Horizontal Travel of Center
                                    %Plate in Center Bowl (in.)

%%Vertical Center Plate Movement Due to Rotation

hv=R1*(-cos(beta)+cos(phi));        %Vertical Travel of Center
                                    %Plate in Center Bowl (in.)


%%Determination of Center Plate Insert Geometry from
%%Rotation Requirements Rounding Algorithm for Horizontal Travel
xx=[1/4,1/2,3/4]; %Rounded Measurements in Quarter Inch Increments(in.)

for i=1:length(xx)
    if h>max(xx)   %Assuring Practical Horizontal Travel
        disp('Horizontal Travel too large')
        break
    end
    if xx(i)-h<.25 & xx(i)-h>=0
        hh=xx(i);
    end

end
hh;                 %Rounded Horizontal Travel Distance (in.)

dc=d-2*hh;          %Center Plate Insert Diameter (in.)
tto=1/8;            %Outer Thickness of Center Plate Insert (in.)
phic=asin(.5*dc/R1);%Angle the Center Plate Surface Traverses from
                    %Outside to Vertical (rad.)
phicd=phic*180/pi;  %Angle the Center Plate Surface Traverses from
                    %Outside to Vertical (rad.)
tt=R1-R1*cos(phic); %Thickness from Curvature of Center Plate Surface
                    %from Tip to Middle (in.)
tti=tto+tt;         %Mid Thickness of Center Plate Insert (in.)

%%Output
disp('Center Bowl Insert Design Geometry:')
disp('     ')
disp('Center Bowl Insert Diameter:')
d
disp('Center Bowl Insert Mid Thickness:')
```

```
ti
disp('Center Bowl Insert Edge Thickness:')
to
disp('Interface Radius of Curvature:')
R1
disp('Center Plate Insert Design Geometry:')
disp('     ')
disp('Center Plate Insert Diameter:')
dc
disp('Center Plate Insert Mid Thickness:')
tti
disp('Center Plate Insert Edge Thickness:')
tto
disp('Total Railcar Height Increase:')
DeltaH=ti+tti
disp('Total Rotation of Railcar Body:')
theta1d

%%%%
%   * The Derivation of the relationships between theta1 and
% the existing geometry used a process in which theta1 was set
% equal to theta2 where the angles corresponded to the rotation
% required for side bearing contact and center bowl gap, respectively.
```

D.2 MATLAB Code for Numerical Integration of M_f

```
%%MATLAB Code for Calculation of Friction Moment

clear
clc

syms psi theta real
syms psi theta positive
%%Input
R1=90               %Radius of Curvature (in)
Nv=286000           %Normal Force (lb)
mu=.3               %Friction Coefficient
psi0=4.94           %Psi Bound (deg)
psi0r=psi0*pi/180   %Psi Bound (rad)

%%Surface Area Calculation
Sa=2*pi*int(R1^2*sin(psi),psi,0,psi0r);
Sa1=vpa(Sa,10)      %Surface Area (in^2)

%%Pressure Calculations
p=2*Nv/(pi*R1^2*(1-cos(2*psi0r)))   %Uniform Pressure Acting
                                    %on 2 Bowls (psi)
st=p*mu                             %Fricton Traction (psi)

%Moment Calculations
L=sqrt((R1*sin(psi)*cos(theta))^2+(R1*cos(psi))^2); %Moment Arm (in.)
L=simple(L);
mint=st*L*R1^2*sin(psi);        %Intermediate Calculations
m1=(int(mint,theta,0,2*pi));    %Intermediate Calculations

Mf=double(int(m1,psi,0,psi0r))  %Moment Due to Friction (lb-in.)
```

D.3 MATLAB Code for Friction Coefficient Calculations

```
%%MATLAB Code for Determining Friction Coefficients

clear
clc
close all
format long

%%Import Test Data
%%Column Layout:
%%Time(s)Axial Disp(in)Axial Load(kips)Rotation(Deg)Torque(lb-in)
data=xlsread('Puck12_3_wc',1, 'A:E');

t=data(:,1);            %Time (s)
tstop=30;               %Final Time for Analyzing (s)
p=data(:,3)*-1000;      %Axial Load (lbs)
Pbar=mean(p);           %Average Axial Load (lbs)
rot=data(:,4).*pi/180;  %Rotation (rad)
rotmax= max(rot)        %Maxi Rotation (rad)
tq=data(:,5);           %Torque (in-lbs)

%%Data Plots
plot(t,p)                   %%Axial Load vs. Time
axis([0,30,0,4000])
title('Axial Load vs. Time')
xlabel('Time (s)')
ylabel('Axial Load (lbs)')

figure
plot(t,rot)                 %%Rotation vs. Time
axis([0,30,-0.06,0.06])
title('Rotation vs. Time')
xlabel('Time (s)')
ylabel('Rotation (rad)')
figure

plot(rot,tq,'b')           %%Torque vs. Total Rotation
axis([-0.06,0.06,-800,800])
title('Torque vs. Rotation')
xlabel('Rotation (rad)')
ylabel('Torque (lb-in)')

%%Find maximum rotation to find slope of the unloading line
for i=1:length(t)
    if rot(i)==rotmax;
        irmax=i;
    end
end
irmax
%%Find Coordinates of Points on Unloading Line
for j=irmax:irmax+10
```

```
    tqslope(j-irmax+1)=tq(j);
    rotslope(j-irmax+1)=rot(j);
end
%%Fit data with line
pf=polyfit(rotslope,tqslope,1);
y2=polyval(pf,rotslope);

figure                    %%Plotting Unloading Line and Approximation
plot(rotslope,tqslope)
hold on
plot(rotslope,y2,'r-')
slope=pf(1,1)

plrot=rot-tq./slope;    %%Find Plastic Rotation
figure
plot(plrot,tq,'r')      %%%Torque vs. Plastic Rotation
axis([-0.06,0.06,-800,800])
title('Torque vs. Plastic Rotation')
xlabel('Plastic Rotation (rad)')
ylabel('Torque (lb-in)')

%%Calculating Energy
for i=1:length(t)
    if t(i)<=30
    drot=plrot(i+1)-plrot(i);
    E(i)=(drot)*(tq(i+1));
    iend=i;
    end
end
%%Dividing Total Energy by Number of Cycles
E=sum(E)/30
%%Calculate Friction Coefficient
mu= 1.5*E/(2*rotmax*1*Pbar)
```

VITA

Name:	Brett Alan Story
Address:	609-E CE/TTI Building Zachry Department of Civil Engineering Texas A&M University 3136 TAMU College Station, TX 77843-3136
Email Address:	bstory@tamu.edu
Education:	B.S., Civil Engineering, Texas A&M University, 2005 M.S., Civil Engineering, Texas A&M University, 2007